Heritage Science

RESEARCH

Open Access

Complementary scientific techniques for the study of Mesoamerican greenstone objects

Willow Knight[1*], Faith Gantz[1], Matthew Carl[1], Marcus L. Young[1], Brigitte Kovacevich[2], Dawn Crawford[3], Elena Torok[4] and Fran Baas[4]

Abstract

Jade and greenstone objects have been held in high regard by many cultures stemming from their limited geological availability and their unique optical and mechanical properties. Jade and greenstone objects symbolized life, fertility, and eternity to early Mesoamerican people. In recent years, scientific studies on jade and greenstone objects have been performed to establish provenance and usage, identify composition, and verify the presence of a particular material. These studies of jade and greenstone objects are generally divided geographically, with considerable interest in China and Central America. Most studies are focused on objects from one particular archaeological site; however, a few studies have focused on collections from a range of sites. The use of multiple complimentary analytical techniques has been shown to be the most effective method for characterizing and understanding the technical information obtained from cultural heritage objects. In our study, we examine a set of Mesoamerican jade and greenstone objects from the collection at the Dallas Museum of Art using multiple non-destructive techniques, including scanning electron microscopy with energy dispersive spectroscopy, Raman spectroscopy, X-ray diffraction, and handheld X-ray fluorescence spectroscopy. We briefly discuss the advantages and disadvantages of each technique. Lastly, we present the results from our study and discuss them in their archaeological and historical context.

Keywords Greenstone, Jade, Mesoamerica, Non-destructive, Non-invasive

Introduction

Jade and greenstone objects are of particular interest due to their prehistorical and historical cultural value which stems from their limited geological availability and their unique optical and mechanical properties. For example, Mesoamerican peoples held greenstone materials in high regard as their hardness, workability, and color were considered symbols of life, fertility, and eternity [1–7]. Scientific characterization of these objects can provide valuable cultural heritage information to museum curators, conservation scientists, and archaeologists [8, 9]. For example, in recent years, studies on jade and greenstone objects have been performed to establish provenance and usage [10], to identify composition [11], and to verify the presence of a particular material [12]. These studies of jade and greenstone objects are generally divided geographically, with considerable interest in China [13–21] and Central America [4, 7, 10, 12, 22–26]. Most of these studies are focused on objects from one particular archaeological site; however, a few studies, including the current one, focus on collections from a range of sites [23, 24, 27, 28]. Scientific studies on greenstones typically

*Correspondence:
Willow Knight
willowknight@my.unt.edu
[1] Department of Materials Science and Engineering, University of North Texas, 1155 Union Circle, Denton, TX 76203, USA
[2] Department of Anthropology, University of Central Florida, 4000 Central Florida Blvd. Howard Phillips Hall 309, Orlando, FL 32816, USA
[3] Department of Anthropology, Southern Methodist University, 3112 Daniel Hall, Dallas, TX 75275, USA
[4] Dallas Museum of Art, 1717 N Harwood St., Dallas, TX 75201, USA

involve at least one characterization technique to identify the minerals present as well as the determination of elemental composition. Characterization of greenstones, especially when their origin is known, can provide information on the development of social complexity and influence of leaders [10, 29], trade patterns [10, 29, 30], and/or significance of buildings, locations, and people [10, 22, 29, 31]. This cultural information allows for a better understanding of the greenstones and provides the ability to reconstruct trade routes and relationships between groups in the past. Before discussing the scientific context, it is necessary to give some historical context for jade and greenstone objects.

Historical context and background

The Spanish colonial term for many Mesoamerican greenstones was *piedra de yjada*, interpreted as "colic stone" [32], but more literally meaning "side" or "flank" after the Aztecs claimed the stone had curative properties on the kidneys, liver, and spleen [33]. *Yjada* eventually transformed into the word "jade", which is internationally present under the name jade. Ethnohistoric studies from Mesoamerica found that indigenous populations made distinctions between varied types of greenstone [34, 35]. The change in terms would describe the color, transparency, quality, and use of the greenstone. For example, *Quetzalchalchihuitl*, ("Quetzal greenstone") translates to be a transparent, "precious" stone with minimum imperfections, and *Chalchihuites* (or more properly *xalxihuitli,* meaning "herb-colored jewels" in Nahuatl, the language of the Aztecs and other Nahua peoples) are known as a good-quality opaque green stone. The differentiation between greenstones suggests that the Aztec and other Mesoamerican cultures viewed each stone type as holding different value [24, 25].

Jade is a general name for mineralogical stones that commonly have a green appearance and can include two minerals called jadeite and nephrite. Ancient Mesoamerican cultures had more interest in jadeite [26, 36]. Jadeite is extremely rare due to the conditions required for its formation. The Motagua River Valley in Guatemala is the only known jadeite sources in Mesoamerica [25]. Jadeite is a monoclinic pyroxene mineral with a structural formula of ($NaAlSi_2O_6$). The addition of other elements to the jadeite composition results in a variety of colors, such as blue, white, black, lavender or the highly valued green, based on elemental substitutions [36]. For example, the elemental presence of nickel and chromium result in a darker green color [25]. The differentiation between the types of jadeites and other pyroxene minerals is a result of coupled substitution, for example, omphacite forms where sodium and aluminum are replaced by calcium and magnesium. Jadeite can breakdown further in wet environments to form analcime or albite [37]. Many Mesoamerican artifacts are a mixture of jadeite and related minerals, like albite, omphacite, diopside, etc., and can be characterized as less than 90% pure jadeite [25, 36, 37]. This study supports these conclusions.

The application of the term "jade" to non-jadeite greenstones has been described as "social jade" [32]. Male burials at the Maya site of Cuello, Belize often contained jadeite while others contained "social jade," suggesting that the ancient Maya could differentiate between jadeite and other greenstones [37], possibly by using basic hardness tests that are still sometimes employed today. Other greenstones worked by ancient crafters are often confused with jadeite by modern scholars, as noted by Hammond and earlier researchers [32]. Many non-jadeite greenstones are deemed inferior for their different workability and luster properties. The hardness of jadeite is very high (6.5–7.0 on the Mohs scale), whereas some of the non-jadeite greenstones such as soapstone or serpentine include much softer minerals (2.5–3.5 and 1.0, respectively). Thus, the most prized properties of jadeite consist of a combination of the stone's hardness, workability, toughness, and lustrous appearance when polished. Some of the other common non-jadeite greenstones include agate, amazonite, muscovite, and jasper [24]. Non-jadeite greenstones have been found in royal tombs, and ceramic beads painted to look like jade at the site of Piedras Negras suggest that the color and symbolism of jade was so desirable that imitations were created and used [24]. These observations have led archaeologists and museum conservators to examine the mineralogical composition more thoroughly. Distinguishing between jadeite and associated greenstones often requires complimentary characterization techniques due to their similar elemental compositions. For example, the differences between jadeite ($NaAlSi_2O_6$) and albite ($NaAlSi_3O_8$) are nearly indistinguishable with elemental techniques such as XRF spectroscopy and EDS, while structural techniques such as XRD and Raman spectroscopy are more telling. However, the differences between jadeite ($NaAlSi_2O_6$) and omphacite ($(CaNa)(MgFe^{2+}Al)Si_2O_6$) are more easily distinguishable with elemental techniques due to the presence of other elements, while structural techniques are less clear since the phases are nearly identical structurally. Furthermore, the choice of analytical technique must also consider the preservation of the cultural heritage object [38, 39]. For example, an ideal analytical technique would meet the following criteria: (1) *non-invasive or non-destructive* (i.e. minimal or no sample preparation, e.g. no pulverization, which is commonly used for powder X-ray diffraction), (2) *fast* for study of a large number of objects, (3) *universal* (i.e. also minimal or no sample preparation, again for a study

of a large number of objects), instrument cost must not be prohibitive, or, for example, the object or the instrument must be transportable or the object must be able to fit within the experimental chamber and accommodate the instrument requirements, (4) *versatile* (e.g. able to collect both local and average properties, (5) *sensitive* (i.e. the measurement must have high enough resolution to be able to distinguish between elements or phase), and (6) *multi-elemental/able to examine multiple phases* (i.e. able to collect information on multiple elements or phases with a single measurement) [38, 39]. Careful consideration of each technique and its requirements is necessary to determine which techniques can be coupled to best address these challenges. Ultimately, multiple complementary analytical techniques in which both phase and elemental compositions are obtained, is truly the only way to clearly differentiate and characterize these minerals and greenstones.

Scientific context

A key goal of many scientific studies on greenstones is to identify the different minerals present, so the objects can be properly categorized and to increase general data on greenstones in Mesoamerica. For example, Gendron et al. [22] verified and quantified the presence of jade in ceremonial axes at an Olmec archaeological site in Mexico. These scientific studies also provide information about the provenance of greenstone objects in Mesoamerica [10, 12, 29, 31]. Better determination of source and provenance of jade in Mesoamerica could be achieved with more research on greenstone geological deposits and associated archaeological sites [31, 40]. Much of the knowledge of mining sources for greenstones in Mesoamerica was lost to history due to European colonization and their disinterest in the stones [12, 41]. It was previously thought that greenstone objects in Mesoamerica originated from China, but it has since been accepted that there must have been some local sources for greenstones found in Mesoamerica. For example, Gendron et al. [12] used Raman spectroscopy to identify a river pebble from Guatemala as a petrological kind of jade not found in China.

Different geological studies determined that jadeite in serpentinite mélanges in the North and South Motagua Fault System Guatemala Suture Zone were resultant of geological collision events and formed during subduction [42–45]. For jadeite found in the Chuacus complex in Guatemala, the case is similar [46]. Jadeite is found in high pressure—low temperature areas in the serpentinite mélanges [42, 44]. It is predicted that jadeite formed in serpentinite as a result of precipitation of and/or metasomatism by aqueous fluid from subduction-zones [43–45]. Compositions of the isotopes of Mg and Li can be used to differentiate between samples and their potential sources as well as give insight into geological events [47, 48].

Non-invasive techniques are preferred for greenstone objects to maintain the integrity of historically and culturally significant objects [23, 41] and these techniques provide sufficient information to characterize greenstones [23]. Some of these techniques include Raman spectroscopy, Fourier-transform infrared spectroscopy (FTIR), X-ray diffraction (XRD), X-ray fluorescence spectroscopy (XRF), and scanning electron microscopy (SEM) with energy dispersive X-ray spectroscopy (EDS) [10, 12, 22, 23, 29, 31, 41]. Like our study, often a variety of the previously mentioned non-invasive techniques are used in combination to study greenstone objects and their performance is compared [23, 31, 41]. While many techniques are suitable for characterizing greenstone objects, portable devices are especially useful as they offer the possibility of in situ analysis without relocating the object [22, 29]. Manrique-Ortega et al. [29] proposed a method of non-destructive analysis of jadeite-jade and evaluated a number of techniques. The study showed that FTIR, Raman, and XRF spectroscopies were capable of rapid analysis and provided sufficient information for characterization, with Raman and FTIR providing mineral identification and XRF providing elemental composition information [29]. These techniques proved to be acceptable alternatives to specific gravity measurements, an invasive petrography technique, and SEM–EDS [29]. The study also showed that particle-induced X-ray emission (PIXE) was another viable non-invasive technique to find elemental composition although it is not portable and has other limitations. In evaluating the techniques, they did point out that Raman spectroscopy, used in the current study, can have drawbacks like high luminescence background, and relatively low resolution and efficiency [23]. Another disadvantage of Raman is that there is not an abundance of reference data or a comprehensive library for mineral spectra, which makes identification more difficult [49]. Advantages of Raman spectroscopy, especially for mineralogical studies, include portability for out-of-lab analysis and sample preparation is not required for analysis [49]. However, high surface roughness can affect spectroscopic characterization by causing spectral changes, so using smooth areas of an object is recommended to avoid these changes [50]. More than just for the sake of comparison, it is often necessary to use a combination of techniques to extract all the necessary information from greenstones. For example, Aguilar-Melo et al. [31] performed XRD and XRF on greenstone objects that had mineral composition mixtures that could not be easily determined using FTIR and Raman spectroscopies.

In addition to the identification of minerals, quantification of the at% jadeite-jade is also of interest when conducting greenstone characterization studies [22, 51]. Gendron et al. [22] derived an equation to find the at% Jd in an object to verify the presence of and then quantify the jade in ceremonial axes from the Olmec culture; this equation was adapted and used in a previous study by Kovacevich et al. [28] and our study presented here.

In our current study, we present results from a variety of analytical techniques such as Raman spectroscopy, XRD, handheld XRF (HHRXF), and SEM with EDS to characterize an array of greenstone objects that belong to various Mesoamerican cultures and are from collections at the Dallas Museum of Art (DMA), thus providing historical and archeological context for the results and providing scientific details on selected objects from our previous study [28]. We also provide an overview and comparison of the analytical techniques used here.

Handheld XRF spectrometry

The major advantage of using a handheld X-ray fluorescence or HHXRF spectrometer is that it is a non-destructive, portable characterization technique that can be used in the field and at museums with no size restrictions, and it is relatively cost-effective in that the device is often less expensive than other stationary devices. It allows in-house analysis for curators, conservators, and staff to collect data without having to transport the objects. While HHXRF spectrometry has many advantages over other analytical techniques, some limitations do exist [52–61], although most of them can be mitigated to some degree. The main limitation of the HHXRF spectrometer is the need for elemental reference standards and a reliable database of similar materials, in this case jadeite and other greenstone materials, to compare with experimental HHXRF measurements. In this study, we did use some elemental reference standards, but did not create a database for comparison or a calibration dataset that could convert the results to comparable parts per million (ppm) measurements. Therefore, our HHXRF spectrometry data has some limitations in quantification and is only semi-quantitative but is compared and verified with other quantitative techniques. Additionally, HHXRF spectrometry is a surface technique probing only a few hundred microns, meaning that surface treatments can affect the measurements [61, 62], although not always [63, 64]. Moreover, cleaning the surface of jadeite or greenstone objects can lead to removal of materials, as well as removal of residue deposits, which is not desired in many archaeological and museum collections as it may preclude other analyses. It is also unknown if any ancient or modern surface treatments were previously applied and some of the objects have traces of surface paints or residues which also change the composition at the surface. Therefore, in our study, we selected surfaces which already appear relatively clean showing only the stone surface and requiring no cleaning for measurements using HHXRF spectrometry. No surface contamination of results was noted in this study. Another limitation of HHXRF spectrometry is that the test surface itself should be relatively flat, otherwise the signal can be weak and result in poor scattering. The solution to this is to find the flattest surface which is also relatively clean and representative of the jadeite or greenstone. Furthermore, HHXRF spectrometry is limited to elemental information only, due to the fact that it is used to measure the characteristic elemental wavelength of a particular fluorescing X-ray. XRF can only infer information about the electronic, chemical, or atomic arrangement. This limitation can be overcome when coupled with other analytical techniques like Raman spectroscopy or XRD, which do provide information on electronic, chemical, and atomic arrangement. For example, Raman spectroscopy provides chemical information about the molecular bonding and symmetry based on vibrational and rotational energies associated with the various compounds within an object, while XRD provides information about the phases present which indicates the atomic arrangement of each individual compound in the object. Thus, coupling these techniques allows for identifying the elements present from HHXRF and then determining their chemical and crystallographic arrangement based on Raman spectroscopy and XRD. Lastly, the HHXRF is ineffective at detecting lighter elements, such as Na and Mg which are crucial elements in the analysis of jadeite and other greenstone objects as they can differentiate closely related minerals like jadeite and serpentine. This limitation can be overcome by adjusting the HHXRF setup to windowless in a vacuum or helium environment. In this study, a helium flow meter was used to overcome this limitation and to detect the lighter elements present in jadeite and other greenstone objects. This technique allowed for the measurement of 67 objects with the HHXRF spectrometer within two and a half days [28]. Here, we present eight of these objects which were further characterized using complementary analytical techniques.

Complementary techniques to HHXRF spectroscopy

The use of multiple complimentary analytical techniques has been shown to be the most effective in characterizing and understanding the technical information for cultural heritage objects [39, 65–70]. Techniques such as SEM to examine an object's surface topography and microstructure, Raman spectroscopy to obtain chemical information at a molecular level, XRD to determine the crystal structure and phase present, and HHXRF and EDS to

identify elemental composition of the objects, are common for cultural heritage research and share a few attributes important for the study of cultural heritage objects; they are non-destructive, are capable of simultaneously examining multiple phases/elements, require minimal sample preparation, collect data quickly, and are highly adaptable and sensitive [39]. This combination of techniques allows for very thorough characterization and exhibits the usefulness of applying diverse methods to a common goal.

Since these objects are irreplaceable, they were scientifically analyzed using the same principles as art conservators, that is mainly: (1) non-destructive/non-invasive handling and analysis, (2) reversibility if treated and possible, and (3) recording/documentation of all basic data. Additionally, some of the techniques involve microscopic measurements which are visually undetectable. Therefore, with this aim, only non-destructive or non-invasive sample preparation was performed on any of the objects and a majority of the object handling was performed by representatives from the DMA to ensure that safe practices were followed throughout the duration of the data collection. Due to the unusual size and shape of the objects, relative to the samples typically analyzed with scientific methods, some objects were unable to be examined using certain techniques and thus no data could be obtained. In addition, before data collection began on objects from collections at the DMA, several pieces of greenstone jewelry of varying shapes and sizes were purchased and used to demonstrate safe practice and determine basic settings for experimental conditions. It was found that all the methods used would have no detectable effect on the structure, color, or integrity of the greenstones as long as proper handling procedures were followed.

Experimental methods

In our initial study, we examined 67 greenstone objects from the collections at the DMA using only HHXRF, as shown in Table 1 [28]. Table 1 indicates the identification of each object based on HHXRF, as jadeite (Jd), predominantly jadeite with omphacite (Jd-Om), predominantly omphacite with jadeite (Om-Jd), omphacite (Om), serpentine (Serp), or inconclusive results (Inc), and also indicates with a "✓" which additional analytical method was performed for each object. In this study, we further analyzed eight of the initial 67 Mesoamerican greenstone objects currently in the collections at the DMA using additional characterization methods including Raman spectroscopy, SEM/EDS, and XRD (see Additional file 1: Supplemental Table 1: Description of Eight Greenstone Objects studied here from the Collections at the Dallas Museum of Art) to gain a deeper understanding of objects. The origin of the objects ranges from southern Mexico, in the modern state of Guerrero, to El Salvador. These objects have been acquired over a period of 40 years from a variety of donors, some anonymous, and vary significantly in size, shape, color, and time period, between approximately 1000 BCE to 300 BCE.

Additional file 1 : Supplemental Table 1 includes a table with the description of eight greenstone objects studied here from ancient Mesoamerica in the collections at the DMA, including accession number, object name, culture, time period, object dimensions, and analytical method, which includes HHXRF spectroscopy (major, minor, and trace elements and result based on the elements present), Raman spectroscopy, SEM, EDS (major, minor, and trace elements and result based on the elements present), and XRD. Note: "Am", "Ant", "Aug", Jd", and "Om" represent the minerals amazonite, anorthite, augite, jadeite, and omphacite, respectively.

Handheld XRF spectrometry

All greenstone materials from the DMA collections were analyzed using a Bruker Tracer III SD HHXRF Spectrometer [71]. The HHXRF spectrometer was attached to a helium tank via a helium regulator. Helium allows for the analysis of lighter elements, like sodium (Na) and magnesium (Mg), which are necessary for the identification of jadeite and to distinguish it from other greenstones [71, 72]. The use of helium, which also makes elements such as aluminum (Al) and silicon (Si) more detectable, requires the removal of the prolene window over the aperture of the HHXRF spectrometer allowing for the helium to cover the distance between the beam and the object itself while preventing the blockage of lighter elements. The HHXRF spectrometer was placed on a metal stand that allowed it to be moved horizontally and vertically, as well as at different angles to better sample the pieces, which vary in size and shape. This also allowed for the HHXRF spectrometer to be placed with the nose/aperture down for the safety of the machine itself when running helium through it. The helium tank with a helium regulator was connected at the vacuum port. The regulator flow rate was set to 0.3LPM prior to connection to the tracer through the vacuum port nozzle. Unlike when analyzing materials without helium and with the prolene window cover, it is not necessary to make sure that the sample is exactly flush or flat against the aperture. Rather, it is better to leave a small 1mm gap between the surface of the object and the aperture to allow for the helium to escape the aperture [71]. All samples were recorded at 15 keV, 25μA, and without a filter in place. XRF spectra were collected for 90 s from each sample measurement, photographs were taken to indicate the

Table 1 Description of sixty-seven greenstone objects studied from the collections at the Dallas Museum of Art

Accession #	Object name	Culture	Time period	HHXRF	Raman	SEM/EDS	XRD
1976.W.248	Pair of ear rods	Cocle	700–1100 CE	Om-Jd			
1973.54	Face effigy	Colima	100 BCE-250 CE	Jd-Om			
2000.238.FA	Crouching male figure	Colima	300 BCE-150 CE	Inc			
1973.55	Hunched seated figure	Colima	100 BCE-200 CE	Om-Jd			
1973.57	Mask with coffee bean shaped eyes	Colima	100 BCE-250 CE	Jd-Om			
1971.42	Pendant: anthropomorphic celt	Greater Nicoya	1–500 CE	Inc			
1973.23	Mask	Guerrero	1200–400 BC	Jd-Om			
2000.236.FA	Monkey	Guerrero	500 BCE-150 CE	Serp			
1973.34	Jade Pendant Depicting a Man's Head	Maya	550–250 CE	Jd	✓	✓	✓
1973.37	Pendant depicting head of ruler	Maya	550–800 CE	Jd		✓	✓
2008.82.4	Bead depicting jaguar head	Maya	600–900 CE	Jd		✓	
2008.79	Plaque fragment with a human head in profile	Maya	600–900 CE	Om-Jd	✓	✓	✓
1973.41	Pendant depicting an enthroned lord	Maya	600–900 CE	Jd			
2008.78	Bead: figure of acrobat or bound prisoner	Maya	600–900 CE	Jd-Om			
1973.42	Jade pendant: contortionist	Maya	250–550 CE	Jd			
2008.81.2	Spherical bead with circles	Maya	600–900 CE	Jd-Om			
2008.76	Pendant: Macaw head profile	Maya	600–900 CE	Jd-Om			
2008.9	Spherical bead with four glyphs	Maya	200–800 CE	Jd-Om			
2008.82.1	Frontal face pendant	Maya	600–900 CE	Jd-Om			
2008.16	Earflare with incised image of principal bird deity	Maya	250–500 BCE	Jd-Om			
1983.W.2	Royal belt ornament	Maya	500–700 CE	Jd-Om			
1973.36	Pendant: head of ruler	Maya	550–800 CE	Jd			
1968.5	Pectoral: supplicant figure	Maya	650–900 CE	Jd-Om			
1973.77	Seated figurine	Mezcala	300 BCE–500 CE	Serp			
1967.11	Standing figurine	Mezcala	500 BC-AD 900	Serp			
1973.44	Seated figure with crossed arms	Mixtec	1100–1500 CE	Serp			
1991.355	Celt	Olmec	1000–300 BCE	Serp	✓		
2000.230.FA	Spoon pendant	Olmec	900–500 BCE	Jd-Om	✓		
2000.232FA	Cylindrical bead depicting a serpent	Olmec	900–500 BCE	Jd-Om	✓	✓	✓
1969.18	Handle for Awl	Olmec	800–400 BCE	Jd-Om	✓		
2000.233FA	Pendant depicting a coiled serpent	Olmec	900–500 BCE	Jd-Om			
2008.86	Bead: monkey profile	Olmec	500–200 BCE	Om-Jd			
1973.75	Pendant: depicting a crocodile	Olmec	900–500 BCE	Jd-Om			
1973.2	Mythological animal	Olmec	900–500 BCE	Jd-Om			
1968.3	Concave pectoral	Olmec	1200–400 BCE	Jd-Om			
2008.81.1	Duck head pendant	Olmec	400–200 BCE	Jd-Om			
1968.16.FA	Hummingbird pendant	Olmec	800–400 BCE	Jd-Om			
1969.5	Pendant: bearded man	Olmec	1200–400 BCE	Jd-Om			
1968.17.FA	Miniature mask	Olmec	800–400 BCE	Jd-Om			
2008.89	Head-form pendant	Olmec	900–500 BCE	Inc			
1969.11	Anthropomorphic plaque, possibly the fire serpent	Olmec	800–400 BCE	Serp			
1973.27	Standing figure with were-jaguar face	Olmec	1200–400 BCE	Jd-Om			
1973.29	Spirit axe	Olmec	900–500 BCE	Serp			
1971.41	Celt	Olmec	900–300 BCE	Jd-Om			
1968.32	Celt with incised plant motif	Olmec	900–500 BCE	Serp			
1973.25	Standing figure	Olmec	900–500 BCE	Serp			
1970.18	Celt with incised masked figure	Olmec	900–500 BCE	Jd-Om			
1968.2	Kneeling male figure	Olmec	800–400 BCE	Serp			
1973.17	Mask	Olmec	900–500 BCE	Jd-Om			

Table 1 (continued)

Accession #	Object name	Culture	Time period	HHXRF	Raman	SEM/EDS	XRD
1983.5	Seated ruler in ritual pose	Olmec	900–500 BCE	Serp			
1973.18	Pendant: Spoon with incised motif in bowl	Olmec	900–500 BCE	Jd-Om			
1973.21	Pendant: reclining figure	Olmec	1200–400 BCE	Jd-Om			
1969.3	Earflare	Olmec	1200–400 BCE	Jd-Om			
1971.73	Earspool	Olmec	1200–400 BCE	Serp			
2008.74	Bead depicting human head	Olmec Style	900–500 BC	X		✓	
1973.26	Standing figure	Teotihuacan	200 BCE-100 CE	Serp			
1973.48	Standing figure	Teotihuacan	100–250 CE	Om-Jd			
1973.5	Face panel	Teotihuacan	250–650 CE	Om-Jd			
1969.4	Double figure	Unknown	600–300 BCE	Serp			
1969.23	Figure	Unknown	600–300 BCE	Jd-Om		✓	✓
2000.241FA	Profile bird head figure	Unknown	1–500 CE	Jd			
2000.240FA	Bird-celt pendant	Unknown	1–500 CE	Inc			
1973.46	Pendant: ruler with jaguar headdress	Unknown	550–800 CE	Inc			
1977.2	Celt	Unknown	1000–1500 CE	Jd			
2004.53	Profile figure holding staff with bird	Unknown	300–700 CE	Jadeite			
2000.234.FA	Standing figure	Unknown	500 BCE-150 CE	Serp			
2000.235	Standing stone figure	Unknown	500 BCE–150 CE	Om-Jd			
1977.3	Tubular bead	Unknown	1000–1500 CE	Om			

In this table includes accession number, object name, culture, time period, and analytical method, which includes handheld XRF spectroscopy, Raman spectroscopy, SEM, and XRD. Note: "Jd", "Om", and "Serp" represent the minerals jadeite, omphacite, and serpentine, respectively. "Inc" represent inconclusive results. "✓" indicates that the object was studied using a specific analytical technique

areas where data was collected, and if possible, at least two different locations were sampled for each object.

Statistical analyses of XRF spectra

Greenstone objects have not been extensively analyzed with a HHXRF spectrometer. Due to this lack of previous analysis and the absence of a calibration curve for the transformation of photon counts to parts per million (ppm), the vast majority of quantitative approaches utilized when analyzing other material systems, like obsidian [73–75], cannot be completed on greenstone. However, unlike with obsidian, our objective was not to determine the chemical source of the greenstone, instead this technique was utilized with the intention of differentiating jadeite from serpentine, and if possible, jadeite from omphacite and other similar rocks or minerals. Therefore, several qualitative and semi-quantitative analyses were employed to test for possible clustering of certain elements in order to differentiate between types of greenstones. The three major analyses were Bayesian deconvolution, region of interest (ROI), and spectral peak analysis, which will be discussed in the next three sections, respectively.

Bayesian deconvolution of XRF spectra

Bayesian deconvolution was completed with ARTAX software available from Bruker. Through ARTAX, XRF spectra can be corrected through Bayesian deconvolution. By matching spectra with the Bayesian deconvolution curve, spectra can be edited and corrected, allowing for a rigorous qualitative analysis. The results are then analyzed through ARTAX and semi-quantitative data created in the form of net count rates for each element in each spectrum. These net count rates can then be compared between elements for the entire sample to look for statistical relationships between specific elements. In this case, the focus was primarily on elements associated with jadeite, omphacite, and serpentine; specifically, Na, Al, Mg, and Ca.

Region of interest analysis on XRF spectra

ROI is another technique that, while qualitative, produces semi-quantitative results. ROI analysis can reduce variation between peaks and allow for the exclusion of interferences. For ROI analysis, all spectra are uploaded into ARTAX and used to identify elemental peaks which are then labeled. The region of interest is selected for each elemental peak through ARTAX, the peak is highlighted, and the photon counts recorded. This ROI technique can be subjective, resulting in data which can vary slightly between individual measurements, because the region of interest is manually selected. One way to minimize this issue is to have only one person collect the data and interpret all measurements (which was done in this

case). ROI analysis provides gross photon count, net photon count, and background photon count. The net photon count is the difference between the gross count minus the background photon count and counts associated with interfering peaks, determined by the ARTAX software. This data was then run through different statistical programs including JMP and Excel, with a focus on gross photon count for specific elements.

Using the statistical program JMP Pro, bivariate plots were created for the ROI results of the spectra from the DMA greenstone HHXRF analysis. Gross photon counts were used in this analysis. Bivariate plots were first created of different elements in comparison to silicon (Si). Clusters were identified when possible and greenstone types assigned based on Mg and Si, Na and Si, Fe and Si, and Ca and Si. The average of these identifications was recorded as the most likely mineral assignment. These results were compared to the averaged mineral assignment from the bivariate cluster assignments of Na, Mg, and Fe as compared to Si.

Spectral peak analysis on XRF spectra

Spectral peak analysis does not require the use of the program ARTAX but is performed through Excel. PDZ files of the spectra are imported into an existing Excel spreadsheet, in this case the University of Missouri Research Reactor Center (MURR) Database for obsidian provided with the Bruker programs, and then gross photon counts for each element in the spectra are imported. The photon counts can then be analyzed semi-quantitatively as long as all of the spectra in question were collected with the same energy, current, filter, time, and atmosphere. Groups and clusters were then created by comparing the photon counts of different elements to try to differentiate between various greenstone types.

Raman spectroscopy

Raman spectroscopy peaks, which appear in the measured spectra, represent a high amount of scattering at a certain wavelength and thus can be correlated to standard samples to make both quantitative and qualitative conclusions about the molecular structure of the object. Raman spectroscopy is a "fingerprint" based technique in which standard samples must be measured under similar conditions and then compared to experimental spectra to make conclusions about the unknown object, therefore it is imperative that some information is known about the objects prior to analysis. In this study, Raman spectra were recorded using a Thermo Fisher Scientific Nicolet Almega XR tabletop Raman microscope equipped with two excitation lasers, 532 nm and 780 nm. The majority of the spectra were collected using the 532 nm laser, as it generally produces a more intense Raman signal, at varying powers between 25 and 100% of the 150 mW maximum power to produce the best possible spectra during data collection. Care was taken to ensure that these conditions would not damage the objects (see Additional file 2: Raw Data from Raman Spectroscopy including a Note about Non-destructive Testing). Spectra were obtained in the 200–2000 cm^{-1} spectral range for an acquisition time of 2–5 s/frame for 5 or 10 frames. A 25 mm pinhole aperture was also used to reduce spectral noise and provide the best possible spatial resolution without sacrificing acquisition times and intensity. It should be noted that, in addition to the tabletop Raman microscope, a portable Raman system equipped with a 532 nm laser was also used to acquire data; however, it failed to measure enough Raman scattering from the objects to produce a discernable spectrum and therefore these results are not included. Reference spectra for jadeite, omphacite, muscovite, amazonite, nephrite, albite, augite, aegirine, and quartz were obtained from the RRUFF project website [76] and used for comparison with our experimental results.

X-ray diffraction

XRD measurements allow for the non-destructive characterization of crystalline phases by the coherent scattering produce in the atomic planes of the repeating structure, offering a non-destructive way to distinctively identify the phase of the material or, in this case, the mineral. Unlike Raman spectroscopy, XRD patterns can be theoretically simulated by modeling the atomic geometry of the mineral and the experimental conditions, thus allowing for identification of the patterns without the need for standard samples. However, this analysis requires a relatively flat surface and generally only probes the top layer, i.e., hundreds of microns, of the material when using reflection geometry, thus surface alterations, i.e., corrosion or protective finishes, can be misleading when trying to characterize the bulk of the object. In this study, XRD patterns were obtained using a Rigaku Ultima III X-ray diffractometer in reflection mode. A Cu K_α X-ray tube was used, producing an incident wavelength of 1.541 Å, at 40kV and 44mA and data was collected over a 2θ range of 20°–80° at a scan rate of 2 degrees/minute with a step size of 0.02°. XRD patterns were analyzed using commercial software, Jade crystal software [77], for qualitative identification of the greenstones. Upon analysis, only large and higher d-spacing peaks were labeled due to peak overlapping at lower d-spacing, making accurate labeling difficult.

Scanning electron microscopy with energy dispersive X-ray spectroscopy

SEM allows for microstructural imaging of the surface due to atomic density differences. In addition, SEM allows for high magnification imaging not possible with light microscopy methods. Another valuable tool in electron microscopy is the direct coupling of EDS. Similar to XRF spectroscopy, EDS is a spatially-dependent elemental surface measurement, but allows high-resolution chemical composition identification through the detection of characteristic X-rays produced by the interaction of the incident electron beam and the object's chemical structure at the surface. Thus, overall chemical composition or any elemental segregation of particular elements can be directly observed and quantified using this technique; however, due to the limited chamber size, $70 \times 70 \times 50$ mm^3, seven of the eight objects could be analyzed using this method. For this study, a Hitachi TM3030Plus SEM equipped with an Oxford mics F + x-stream-2 EDS detector system was used for imaging and compositional analysis, respectively. Quantitative element compositions were analyzed using Oxford AZtec software. The SEM was operated using 15kV voltage under low vacuum at a working distance ranging between 7.5 and 13.6 mm with scan image dwell times and EDS map dwell times of 5 µs and 100 µs, respectively.

Results

Additional file 1: Supplemental Table 1 summarizes the data collected for each object that was studied using additional analytical methods other than HHXRF spectroscopy, while Figs. 2, 3, 4, 5, 6, 7, 8 and 9 show these objects and corresponding data collected using additional techniques.

Handheld X-ray fluorescence spectrometry

Nearly every Mesoamerican greenstone object in the DMA collection (N = 67; Table 1) (see also Additional file 3: Artax2 Raw Data from HHXRF Spectroscopy) was characterized by HHXRF as it is a relatively quick, non-destructive process that does not have sample size restrictions. The readings can be taken within the museum and there was no need to remove the objects from display because the device is small and portable. HHXRF was used initially to differentiate between serpentine and jadeite/omphacite; this technique does not have the sensitivity to identify different members of the serpentine family (i.e., antigorite, lizardite, chrysotile). Of the 8 objects selected for further analysis and discussion in this article, none were identified as serpentine. Another item from the museum collection, Celt (1991.355), underwent further analysis and was identified by HHRXF as serpentine, though results of further analyses for the object were inconclusive and need further study; see discussion in [28]. Nevertheless, differentiation of jadeite and other minerals like omphacite was productive and HHRXF shows promise for differentiating different types of greenstone. Objects were compared to known samples of jadeite, omphacite, and serpentine, but certain elements were more diagnostic than others in the bivariate plots used to determine group membership, as shown in Fig. 1. For example, jadeite ($NaAlSi_2O_6$) can be indicated by the presence of sodium with less magnesium, calcium, or iron. In contrast, omphacite ($(CaNa)(MgFe^{2+}Al)Si_2O_6$) includes sodium, with higher levels of magnesium, calcium, and iron as primary identifiers, whereas the minerals in the serpentine group, which are magnesium silicates, lack sodium and calcium but include higher levels of magnesium. Our results show that the overwhelming majority of these objects are composed of a mixture of jadeite and omphacite, with more jadeite than omphacite (n = 30). The second most represented group was serpentine (n = 15), followed by jadeite (n = 9), omphacite/jadeite with omphacite as the primary mineral (n = 7), and one object appearing to be primarily omphacite. Five objects were not classified and found to have inconclusive results as they did not cluster with any of the groups and may have been a mineral or compound for which we did not have a known sample for comparison. These identifications may not have been possible without the addition of a helium flow meter to amplify the presence of lighter elements like sodium and calcium.

Of the total HHXRF sample set (N = 67), nine of the objects identified as pertaining to Maya culture were a combination of jadeite and omphacite, while six Maya objects were found to be primarily jadeite. Of the objects identified as being from the Olmec culture, 18 were some combination of omphacite and jadeite, while eight were identified as serpentine. Two objects were identified as being from Guerrero, one was jadeite/omphacite and the other was serpentine. Colima objects were a combination of omphacite and jadeite (n = 3) with one inconclusive (n = 1), while objects from Teotihuacan were both jadeite/omphacite (n = 2) and serpentine (n = 1). Other cultures represented were Cocle (serpentine, n = 1), Mixtec (serpentine, n = 1), Mezcala (serpentine, n = 2), Greater Nicoya (inconclusive, n = 1). Five objects were of unknown provenance and were a combination of omphacite/jadeite (n = 2), jadeite (n = 2), and serpentine (n = 1).

While these HHXRF results were promising, again, they were only semi-quantitative, in that a calibration dataset was not developed to compare the DMA objects to known samples and quantify the elemental compositions in parts per million (ppm) measurements. Based on this HHXRF study, we chose 8 objects (see Additional file 1: Supplemental Table 1 and object descriptions in

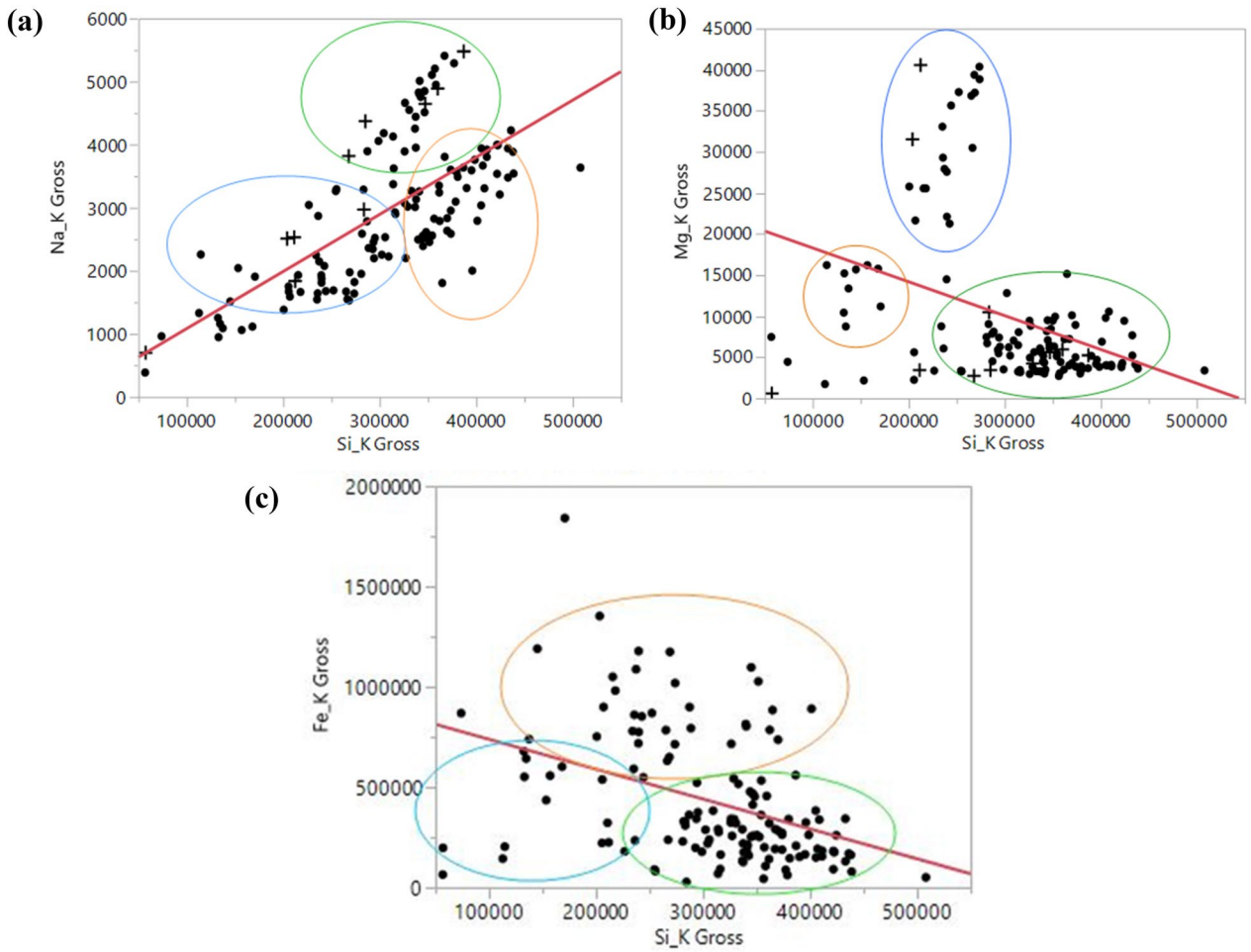

Fig. 1 Bivariate fit of handheld XRF photon counts for all 67 objects in the DMA collections of **a** gross Na by gross Si, **b** gross Mg by gross Si, and **c** gross Fe by gross Si, all after ROI analysis. Ellipses indicate mineral clusters with serpentine in blue, omphacite in orange, and jadeite in green. The "+" symbol indicates the objects that were additionally studied with other techniques presented here. Ellipses are drawn at 95% confidence. Images reproduced courtesy of the Dallas Museum of Art Catalogue Article

the "Discussion" section) for further analysis to compare and possibly confirm our HHXRF results. Generally, our findings were supported by additional characterization techniques, showing that using HHXRF for mineralogical identification of greenstones is possible, but strengthened with the use of additional techniques. With the creation of a calibration dataset and use of reference standards with known compositions, HHXRF could be even more reliable and effective.

Tabletop Raman spectroscopy

Size constraints in the Z-direction of the microscope stage only allowed for examination of four of the eight objects using the tabletop Raman microscope, which includes objects 1973.34, 2008.79, 2000.230.FA, and 2000.232.FA. Raman data for each object was background corrected and compared with reference spectrum such as jadeite and omphacite. Objects 2008.79 (Fig. 2c), 1973.34 (Fig. 3c), 2000.232.FA (Fig. 4c), and 2000.230.FA (Fig. 5b) were collected using the 532 nm laser and show similar Raman spectra with major peaks centered at approximately 369, 430, 522, 575, 695, 984, and 1036 cm^{-1}. However, the peak intensity and minor positions shifts are observed between the sample and do represent important structural and chemical changes in the objects. Qualitatively, the data can be described by the following peak "groups": (1) a triplet group in the range of 280–350 cm^{-1}, (2) an intense peak followed by either a low intensity single peak or doublet at 370–440 cm^{-1}, (3) the major peak around 695 ± 10 cm^{-1}, and (4) a doublet of varying intensity at 980–1040 cm^{-1}. Physically, these peak groups can be quantified by their scattering source and therefore lead to important structural knowledge of the mineral that can be used for definite evidence

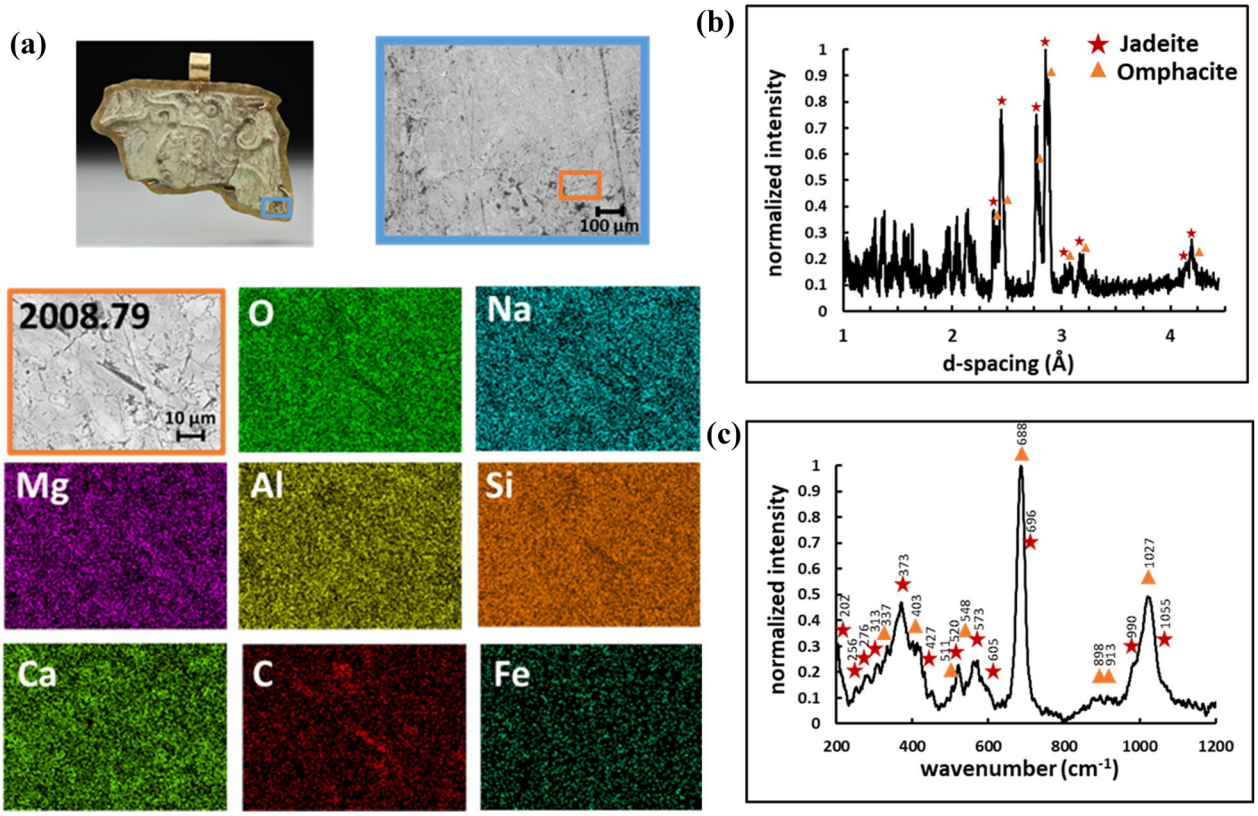

Fig. 2 **a** Photograph of *Plaque fragment with Human Head in Profile* (2008.79) with detailed SEM image (blue box) and more detailed SEM image (orange box) with elemental mapping of O, Na, Mg, Al, Si, Ca, C, and Fe, respectively, **b** XRD pattern, and **c** Raman spectrum

for material identification. Specifically, when discussing clinopyroxenes (NaPx), minerals, such as jadeite and omphacite, the Raman bands outlined above are related to: (1) lattice mode vibrations involving metal–oxygen interactions and possibly O–Si–O bending, 50–400 cm^{-1}, (2) O–Si–O bending modes of the SiO_4 tetrahedron, 400–630 cm^{-1}, (3) vibrations within the silicate chains of Si–$O_{bridging}$–Si, or bridging O atoms, 630–800 cm^{-1}, (4) and lastly the stretching of Si–O bonds in SiO_4 tetrahedrons, 800–1200 cm^{-1} [78]. Knowing this information, it is sometimes possible to semi-quantitatively identify chemical structures based on the position of the peak groups. The application of this analysis will be addressed in the "Discussion" section later in this article.

Laboratory X-ray diffraction (XRD)

Limited availability and size/shape constraints allowed for XRD analysis of five of the eight objects including objects 2008.79 (Fig. 2b), 1973.34 (Fig. 3b), 2000.232. FA (Fig. 4b), 1973.37 (Fig. 6b), and 1969.23 (Fig. 9b) (for raw data, see Additional file 4: Raw Data from X-ray Diffraction Measurements). XRD patterns for each object were normalized and compared with reference spectrum such as jadeite and omphacite. Similar XRD patterns were observed for objects 2008.79 (Fig. 2b) and 1973.34 (Fig. 3b) with the main reflections coming from the peak doublet between the range of 2.8–3.0 Å. The relative intensity of the two peaks is slightly different but this could be because of crystallographic orientation effects within the objects or compositional variance. An important difference in the patterns is seen in the range of 2.4–2.6 Å. In the diffraction pattern for object 2008.79, a distinct triplet peak group is not readily visible in object 1973.34 (Fig. 3b). This triplet peak group helps to illustrate the slight difference within the samples regarding structural composition. It is apparent that crystal structures between the two greenstone phases are closely related and therefore difficult to distinguish; however, in the range of 2.4–2.6 Å, omphacite produces a shifted set of reflections with moderate intensity. Therefore, it is hypothesized that both objects 2008.79 (Fig. 2b) and 1973.34 (Fig. 3b) display some amount of both omphacite and jadeite within the sampled volume and in addition, it is likely that the fraction of omphacite is higher in object 2008.79 (Fig. 2b), since an observable middle peak exist in the d-spacing range of 2.4–2.6 Å, specifically at

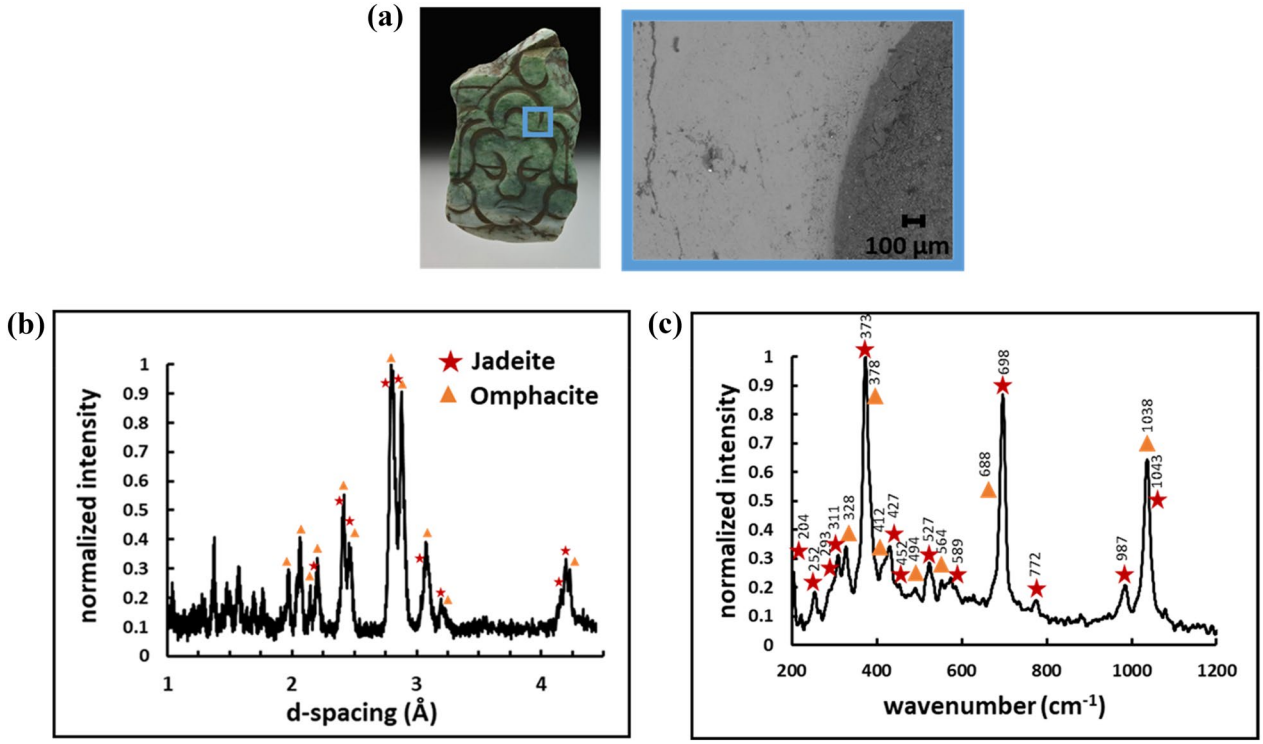

Fig. 3 **a** Photograph of *Jade Pendant Depicting a Man's Head* (1973.34) with detailed SEM image (blue box), **b** XRD pattern, and **c** Raman spectrum

2.46 Å. It should be noted that there also exists a peak doublet at the high d-spacing range, around 4.3 Å, that can help distinguish between the two minerals, but these are of lower intensity and not conclusive in our study. Object 2000.232.FA (Fig. 4b) produces a slightly different but related XRD pattern. The peak doublet at the high d-spacing range is a clear indication of jadeite, although it is observed that there is also some fraction of omphacite based on the triplet group in range of 2.4–2.6 Å that would not appear if the sample were pure jadeite. However, the phase fraction of omphacite in object 2000.232.FA (Fig. 4b) is less than the phase fraction in both objects 2008.79 and 1973.34 (Fig. 3b).

Scanning electron microscopy and energy dispersive spectroscopy

Due to the limited size of the analysis chamber, SEM with EDS was only able to be performed on seven of the objects, including objects 2008.79 (Fig. 2a), 1973.34 (Fig. 3a) (mapping not performed due to the EDS not working at the time of collection), 2000.232.FA (Fig. 4a), 1973.37 (Fig. 6a), 2008.82.4 (Fig. 7a), 2008.74 (Fig. 8a), and 1969.23 (Fig. 9a). The surface of object 2008.79 (Fig. 2a) is smooth with large, faceted crystals of slightly varying brightness in a basically bimodal distribution attributed to minor composition differences within the sample. In addition, large pores are evident across the surface. Object 1973.34 (Fig. 3a) shows a similar surface as object 2008.79 (Fig. 2a) with a bimodal distribution. The surface exhibits a finer textured, mini faceted surface from the crystal growth with many apparent pores of varying sizes but in general smaller than those seen in Object 2008.79 (Fig. 2a). Object 2000.232.FA (Fig. 4a) does not display a bimodal distribution like on the surface of objects 2008.79 (Fig. 2a) and 1973.34 (Fig. 3a), but rather consist of a general matrix phase with large inclusion (approximately 50 microns) present throughout. The surface morphology appears slightly rougher than objects 2008.79 (Fig. 2a) and 1973.34 (Fig. 3a) with large, jagged crystals evident. The surface of object 1973.37 (Fig. 6a) shows a homogeneous and fine mixture of two phases. Object 2008.82.4 (Fig. 7a) shows a similar smooth surface to object 1973.37 (Fig. 6a), with some kind of surface contamination present. Object 2008.74 (Fig. 8a) shows a smooth surface without pores and a coarse mixture of two phases, whereas object 1969.23 (Fig. 9a) shows a fine and more faceted mixture of two phases.

Table 2 presents compositional measurements using EDS during SEM imaging on seven of the eight objects. A point of interest is that objects 2008.79 (Fig. 2a) and 1973.34 (Fig. 3a) display noticeably higher Ca and Mg contents with slightly lower amounts of Na and Al when

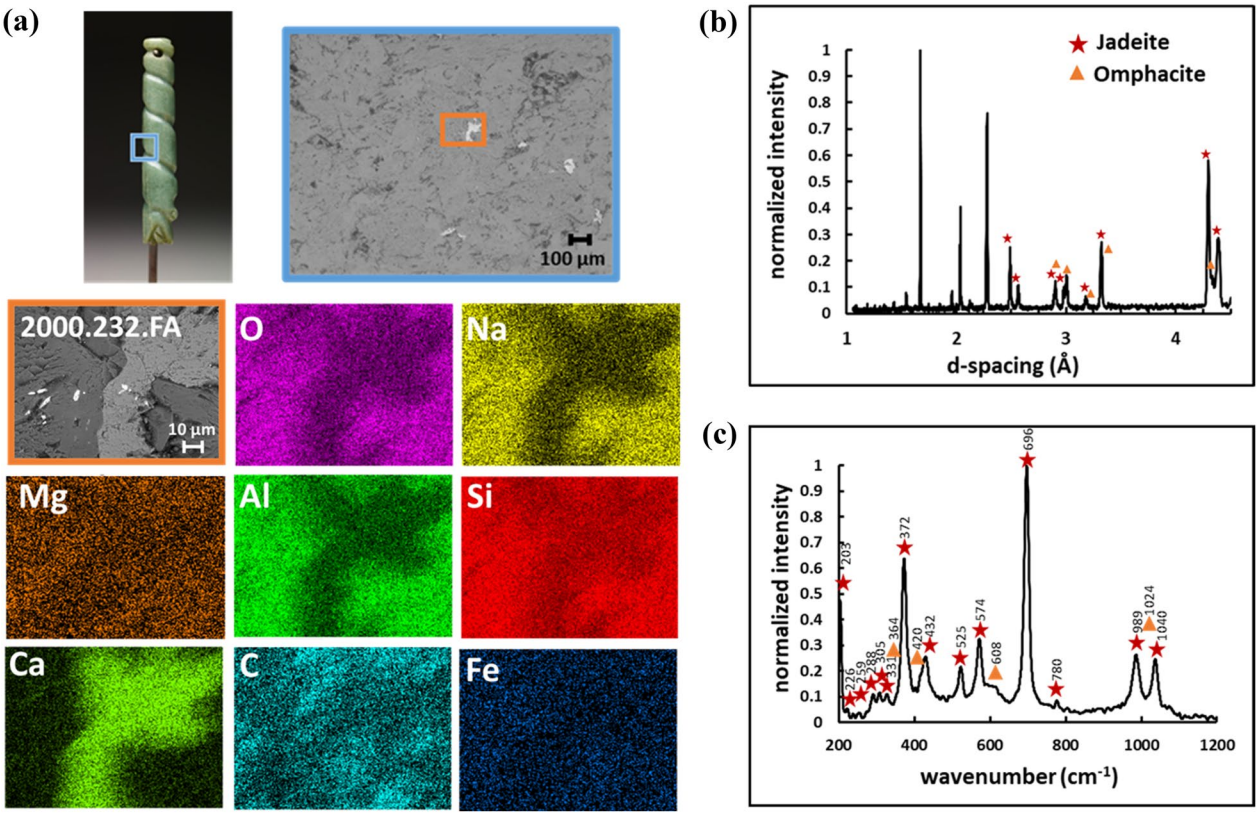

Fig. 4 **a** Photograph of *Cylindrical Bead Depicting a Serpent* (2000.232.FA) with detailed SEM image (blue box) and more detailed SEM image (orange box) with elemental mapping of O, Na, Mg, Al, Si, Ca, C, and Fe, respectively, **b** XRD pattern, and **c** Raman spectrum

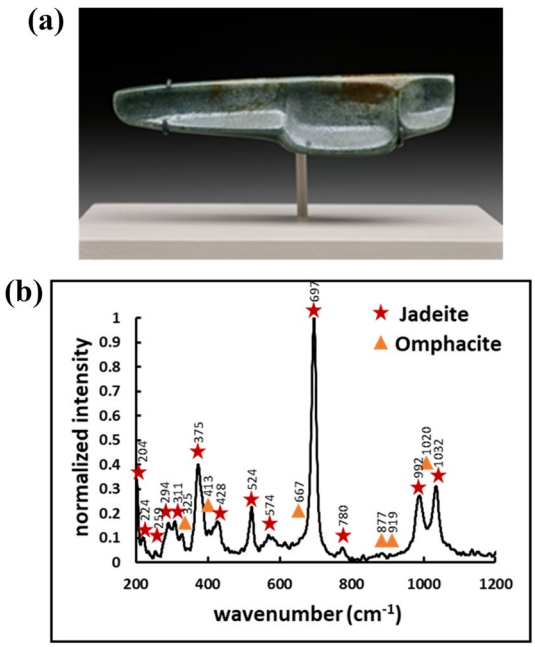

Fig. 5 **a** Photograph of *Spoon Pendant* (2000.230.FA) with and **b** Raman spectrum

compared to object 2000.232.FA. The change in Si, C, and O between the samples is most likely due to surface contaminations, such as organic treatments, residues, or cleaning solutions, which obscure the analysis of the technique and should be taken with caution, especially with the case of 2008.74, which is displaying high fractions of C. C, Si, and O are present in Table 2, but were not considered in the qualitative analysis of the greenstone mineral constituents. Calculations (using the equation in "Plaque fragment with a human head in profile (2008.79)" section) show objects 2000.232.FA and 1973.37 to be the highest percent jadeite, while object 1969.23 shows the lowest percent jadeite.

Discussion

Scientific analysis and summary of results

As previously described, Additional file 1: Supplemental Table 1 summarizes the experimental data collected with each technique for each of the eight greenstone objects. It is now of interest to discuss each object individually based on the analytical information acquired.

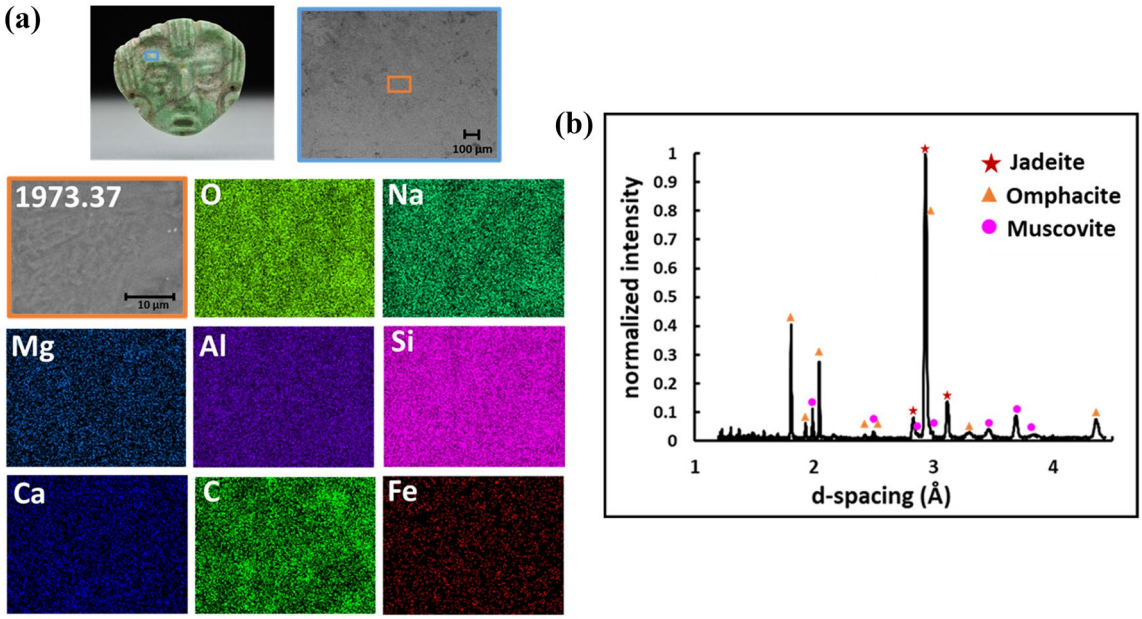

Fig. 6 **a** Photograph of *Pendant depicting head of ruler* (1973.37) with detailed SEM image (blue box) and more detailed SEM image (orange box) with elemental mapping of O, Na, Mg, Al, Si, Ca, C, and Fe, respectively and **b** XRD pattern

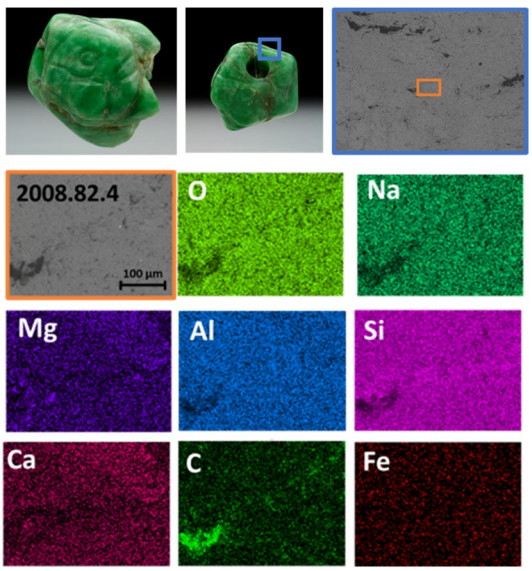

Fig. 7 Photograph of *Bead Depicting Jaguar Head* (2008.82.4), an alternate angle of the object with detailed SEM image (blue box) and more detailed SEM image (orange box) with elemental mapping of O, Na, Mg, Al, Si, Ca, C, and Fe, respectively

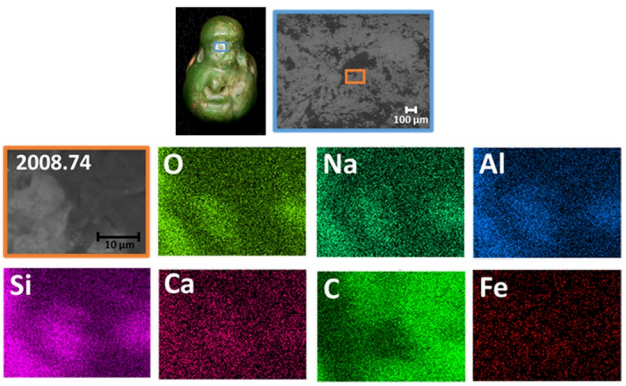

Fig. 8 Photograph of *Bead Depicting Human Head* (2008.74) with detailed SEM image (blue box) and more detailed SEM image (orange box) with elemental mapping of O, Na, Mg, Al, Si, Ca, C, and Fe, respectively

Plaque fragment with a human head in profile (2008.79)

As illustrated in Fig. 2, the relatively small size and flat shape of the *Plaque Fragment with a Human Head in Profile* (2008.79) allowed for the collection of experimental data using all techniques.

Based on the HHXRF data of the *Plaque Fragment with a Human Head in Profile*, the object is identified as jadeite with a relatively large amount of omphacite as indicated by spectral peaks with large photon counts of calcium and iron (present in omphacite, (CaNa)($MgFe^{2+}Al$)Si_2O_6) and magnesium (Additional file 1: Supplemental Table 1). As illustrated in Fig. 1, the Region of Interest (ROI) analysis groups the object as having magnesium and iron readings representative of jadeite, but sodium readings that group it with omphacite [28].

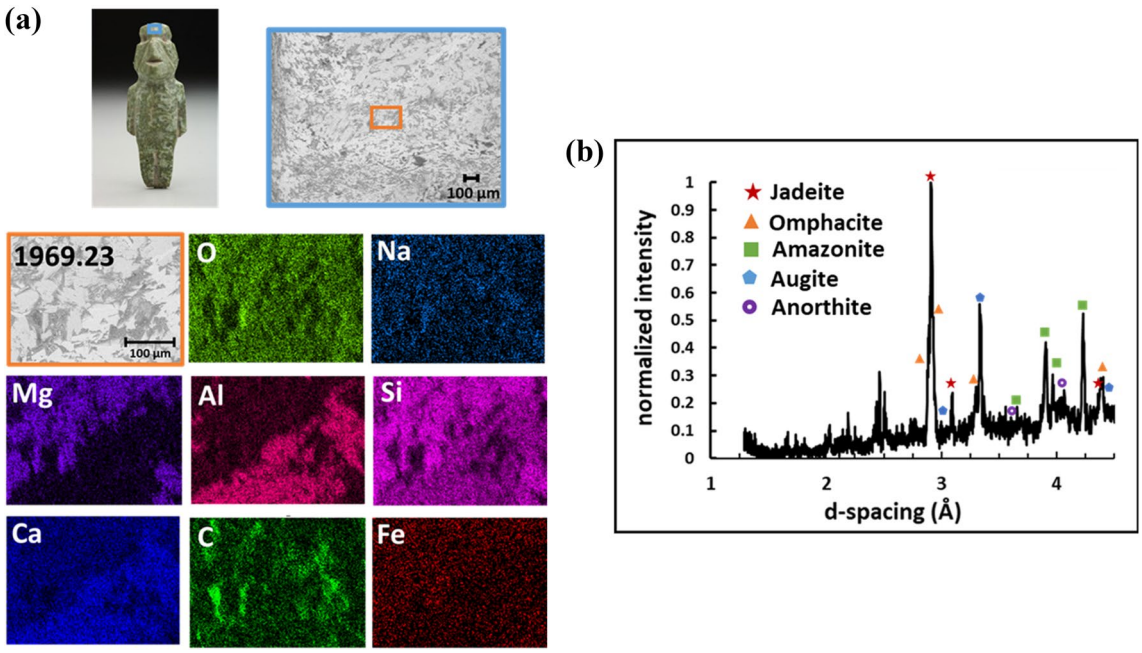

Fig. 9 Figure (1969.23), **a** image of the object with detailed SEM image (blue box) and more detailed SEM image (orange box) with elemental mapping of O, Na, Mg, Al, Si, Ca, C, and Fe, respectively, and its **b** XRD pattern

Table 2 Elemental compositions from EDS measurements

Accession #	at%									$\%Jd_{EDS}$
	O	Na	Mg	Al	Si	Ca	C	Fe	K	
1973.34	52.0 (4.3)	4.6 (0.6)	3.1 (0.5)	4.7 (0.5)	16.9 (2.3)	3.6 (0.5)	18.0 (3.4)	0.6 (0.1)		55.5
1973.37	42.0 (1.2)	4.6 (0.2)	0.5 (0.01)	4.8 (0.3)	10.2 (0.7)	0.4 (0.03)	36.9 (0.03)	0.1 (0.03)	0.4 (0.1)	90.1
2008.82.4	51.0 (1.5)	6.0 (0.3)	1.2 (0.3)	5.4 (0.3)	12.8 (0.7)	1.0 (0.3)	22.3 (2.9)	0.21 (0.03)	0.05 (0.02)	83.2
2008.79	46.2 (2.3)	4.0 (0.5)	1.9 (0.2)	4.2 (0.3)	11.8 (1.4)	2.1 (0.4)	29.1 (5.0)	0.6 (0.1)		64.3
2008.74	24.1 (4.6)	1.6 (0.5)	0.3 (0.1)	1.5 (0.6)	4.5 (1.6)	0.3 (0.1)	67.2 (7.3)	0.12 (0.04)	0.1 (0.02)	81.8
2000.232.FA	44.9 (0.7)	5.1 (0.2)	0.4 (0.1)	5.2 (0.2)	11.3 (0.4)	0.4 (0.1)	32.0 (0.6)	0.4 (0.1)	0.1 (0.03)	91.6
1969.23	37.1 (2.8)	0.4 (1.3)	2.0 (1.2)	4.7 (2.4)	8.0 (0.2)	4.8 (1.2)	41.9 (4.5)	0.5 (0.2)	0.2 (0.1)	41.1

The equation used for the %Jd calculation is described in "Plaque fragment with a human head in profile (2008.79)" section

The Raman spectra is characterized by a single peak at 204, a doublet peak at 372 and 413 cm^{-1}, a doublet at 521 and 573 cm^{-1}, a main peak at 686 cm^{-1}, and finally a doublet at 989 and 1023 cm^{-1} (Fig. 2c). The Raman signature for the plaque fragment does not match either jadeite or omphacite completely and most likely is a mixture of the two mineral structures. The strong scattering intensity at 204 cm^{-1} is due to the presence of jadeite within the object and matches the reference sample; however, as we move into the 350–600 cm^{-1} range, deviations from the reference jadeite arise. The omphacite (Om) and jadeite (Jd) reference patterns show distinct scattering peaks at 375 (Jd and Om), 410 (Om), and 434 (Jd) cm^{-1}, which is relatively close to the 372 and 413 cm^{-1} peaks in the plaque fragment and represents a chemical deviation from the pure structures, e.g. a mixture of the two clinopyroxenes minerals within the sampled volume. By far, the main Raman band used for the identification and quantification of jadeite and other greenstones, in the clinopyroxene family, is the strong scattering signal between 600 and 800 cm^{-1}, or the symmetric stretching of the Si–$O_{bridging}$-Si vibration bands within the mineral [22, 51, 76]. In the pure jadeite reference, this peak is centered at 701 cm^{-1} while omphacite and nephrite show a scattering signal at 678 and 673 cm^{-1}, respectively. The reason for this shift can be explained by the substitution

of the tetrahedron cation species (Fe^{2+}, Fe^{3+}, Mg^{2+}, Na^{+}, or Ca^{2+}) in the Si–$O_{bridging}$–Si structure, which produces a shift in the Raman signature [22, 51]. It is apparent that the peak lies between the reference samples and therefore this implies that the object is neither pure jadeite nor omphacite. In previous Raman greenstone studies, it has been shown with reasonable accuracy that the at% of jadeite-to-omphacite can be given by the following equation since the two structures can exhibit a solid solution [12, 22, 51]:

$$Jd\% \approx 100 - \{[703 - W] \times 2.5\}$$

where W is the wavenumber in cm^{-1} for the Si–$O_{bridging}$–Si peak. Applying this equation to the plaque fragment yields a result of approximately 57% Jd in the sampled area. It should be noted that this is a mere estimation and only semi-quantitative but none-the-less, still provides meaningful information in the composition and structure of the object. This large deviation in peak position, and therefore lower jadeite percentage, implies that omphacite is a significant constituent. The final peaks present in the Raman signature also lean more towards an omphacite composition as the stretching of the Si–O bonds in the SiO_4 tetrahedron are pushing closer together and producing one scattering signal rather than two distinct peaks as seen in the jadeite reference. XRD for object 2008.79 in Fig. 2b. also supports the position that the object is a mixture of jadeite and omphacite. The crystallographic structural difference between jadeite and omphacite is slight, but meaningful. As omphacite cations (Mg, Fe, Ca) are added to the pure jadeite, they begin to replace the Na and Al create a change in the crystal symmetry [78]. Therefore, the reflections are shifted and, in some cases, spilt into pairs or not observed. The low intensity, sample orientation, and difficult experimental setup make absolute measurement of the crystal lattice and phase fraction difficult and, therefore, will not be presented here. However, a qualitative understanding of the object can be gained. It is clear that only a single peak exists in the high d-spacing range, which supports but does not verify the absence of jadeite entirely from the sample. Solidification and processing methods play an important role in the observed intensity of certain reflections in XRD experiments and can lead to distorted information if not properly accounted for during analysis. Therefore, peaks must be analyzed in groups and the XRD pattern for the plaque fragment shows possible reflections for both omphacite and jadeite, most visible in the range of 2–3.5 Å. This leads to and supports the hypothesis from the Raman analysis that the object is likely a mixture of omphacite and jadeite. As illustrated in Fig. 2a, the SEM image of the surface shows a bimodal distribution in the brightness of the matrix phase in the plaque fragment. This can be attributed to segregation of specific elements, although not quantified in this report. The brighter facets visible indicate a higher atomic density within that region, i.e. the brighter facets contain higher atomic weight elements. Considering the compositions of jadeite, $NaAlSi_2O_6$, with respect to omphacite, (Ca, Mg, Fe)Si_2O_6, the substitution of Ca, Fe, and Mg cations for the original Na and Al cations would cause a higher amount of backscattered electrons and therefore create a brighter region in the SEM image. This is directly observed in Fig. 3a for object 2008.79 with brighter regions representing the omphacite phase and darker regions representing the jadeite phase. This contrast difference has been reported by other researchers as well and attributed to the same phases [23, 41]. Quantitative EDS measurements of the surface region show that there is an appreciable amount of Mg and Ca within the material (Table 2). In order to show a qualitative relationship between jadeite and omphacite, the following equation was developed based on the ideal compositions $NaAlSi_2O_6$ and (Ca, Mg, Fe)Si_2O_6:

$$\%Jd_{EDS} = (Na + Al)/(Ca + Mg + Fe + Al + Na)$$

This leads to an estimation of 64% Jd from the plaque surface, which is in decent agreement with the Raman estimation. Which is in the area of approximately 60% Jd–40% Om. Based on the criteria set by Gendron et al. [12, 22], the object is classified as an omphacite-jade gemstone, which is in general agreement with the HHXRF readings.

Jade pendant depicting a man's head (1973.34)

As illustrated in Fig. 3, the *Jade Pendant Depicting a Man's Head* (1973.34), also allowed for extensive examination due to its small size and relatively flat shape.

Based on the HHXRF data and photon counts of the *Jade Pendant Depicting a Man's Head,* the presence of calcium, iron, and traces of sodium suggests the object contains a mixture of mostly omphacite with some jadeite (Table 2), while the ROI analysis shows the presence of magnesium, sodium, and iron suggesting the object primarily consists of jadeite. These two results indicate that the object is likely a mixture of jadeite and omphacite, with jadeite as the major component. Raman spectroscopy produced a clear Raman signal with peaks at 204, 256, 309, 328, 373, 428, 523, 696, 988, and 1036 cm^{-1} (Fig. 3c) The pattern clearly identifies with the clinopyroxene minerals and shares many peaks with the jadeite reference sample; however, the peaks are slightly shifted to a lower wavenumber emphasizing again the substitution of the Al and Na cation species for Fe, Mg, and Ca. Employing the same methods as above it is predicted by the peak at 696 cm^{-1} that the mineral is approximately

83% Jd–17% Om. XRD pattern in Fig. 3b shows a mixture of both omphacite and jadeite, which is incidentally similar to the XRD pattern of *Plaque Fragment with a Human Head in Profile (2008.79)* (Fig. 2b). Although important differences are observed, mainly in the relative intensity of the peaks between 2.5 and 3 Å. Examining the reference patterns, it is observed that the symmetry caused by the omphacite phases creates a split peak opposed to a single peak at 2.8 Å and therefore lowering the observed intensity of the doublet. Comparing the XRD pattern from object 2008.79 to the pattern in object 1973.34, it is clear that some asymmetry exists in the peak at 2.8 Å and related to a shoulder peak resulting in a high fraction of omphacite with respect to jadeite. This asymmetry is not clearly apparent in the XRD pattern for *Jade Pendant Depicting a Man's Head* and therefore it is hypothesized that the percentage of omphacite is less in the pendant than in the plaque fragment. This position is also supported by the Raman data as already discussed. SEM imaging of the surface shows two regions, a lighter region and a darker region, the latter likely consisting of organics on the surface which were used as colorants. The lighter region shows a bimodal distribution related to pockets of segregation from the omphacite type cations (Fig. 3a). The segregation is not as clear in the pendant as in the plaque fragment, but still of noticeable levels. EDS measurements again show some amount of Ca and Mg adding to the conclusion that omphacite is present in the object (Table 2); however, using the % Jd_{EDS} equation a large discrepancy exists between the Raman estimation and the EDS measurements. The qualitative EDS equation yields approximately 56% Jd–44% Om. Since the EDS estimation is untested and Raman is known to predict accurate results within 5 at% [12, 22], the Raman measurements should be taken with higher confidence. Thus, based on the analysis, the Jade pendant is approximately 80% Jd–20% Om and has jadeite as a major component.

Cylindrical bead depicting a serpent (2000.232.FA)

As illustrated in Fig. 4, the *Cylindrical Bead Depicting a Serpent* (2000.232.FA) allowed for all experimental techniques to be used due to its small size, although the curved shape is not ideal.

The HHXRF spectra from the *Cylindrical Bead Depicting a Serpent* object indicated that the object primarily consists of iron, with traces of sodium and magnesium (Additional file 1: Supplemental Table 1), thus ROI analysis points to predominantly jadeite with some omphacite [28]. Raman spectroscopy shows defined peaks at 204, 256, 311, 328, 374, 428, 521, 574, 699, 778, 984, and 1038 cm^{-1} correlating with the pure jadeite patterns and minor lowered wavelength shifts in the primary peaks (Fig. 4c). The % Jd based on the 699 cm^{-1} peak is approximately 90% Jd–10% Om. XRD pattern indicates mostly jadeite but with a minor shift in peak positions likely due to substitutional atoms within the crystal structure (Fig. 4b). The XRD pattern displays the correct symmetry group for jadeite rather than omphacite, but reflections that are not cohesive with pure jadeite references are observed to be related to some amount of omphacite, which is supported by the Raman signature. The surface observed with SEM looks relatively homogenous with respect to the matrix phase and no micro-segregation was observed (Fig. 4a). However, a small number of large inclusions with appreciable amounts of Ti and Zr were observed, but not representative of the sample, so they are not present in the EDS results presented in Table 2. EDS compositions show only minor amounts of Ca, Mg, and Fe and % Jd_{EDS} was estimated to be approximately 90% Jd–10% Om, in good agreement with Raman estimations (Table 2). Although still predominantly jadeite with omphacite, the HHXRF results indicate that omphacite has a more significant representation, as compared to all other analysis. This demonstrates the limitations of using the HHXRF alone. Aside from HHXRF, all other techniques, i.e., Raman spectroscopy, XRD, SEM, and EDS, indicate that this object consists predominantly of jadeite (e.g. ~ 90% jadeite for both Raman spectroscopy and EDS) with a small amount of omphacite. Again, the results of the HHXRF and other techniques generally agree, although the additional techniques provide more quantitative and detailed results.

Spoon pendant (2000.230.FA)

As illustrated in Fig. 5, the *Spoon Pendant* was large in length (Fig. 5a), which led to difficulty in using SEM and XRD for analysis. Therefore, only HHXRF and Raman data were obtained in this case.

The HHXRF analysis of the *Spoon Pendant* suggests the presence of omphacite due to iron serving as a major element, with a minor amount of calcium and traces of sodium (Additional file 1: Supplemental Table 1). In contrast, the ROI analysis points to predominantly jadeite with some omphacite due to the high amount of magnesium and iron with only a small amount of sodium, respectively [28]. *The Spoon Pendant* produced a clear Raman signature of a clinopyroxene mineral with peaks being observed at 204, 290, 306, 374, 425, 521, 695, 989, and 1035 cm^{-1} (Fig. 5b). The pattern closely identifies with the jadeite structure with minor peaks shift to lower wavenumbers, like those observed in objects 2008.79, 1973.34 and 2000.232.FA. The % Jd is estimated to 80% Jd–20% Om (Table 2). Thus, the object is a lower purity jadeite and can possibly be classified as an omphacite-jadeite greenstone.

Pendant depicting head of ruler (1973.37)

As illustrated in Fig. 6, the *Pendant Depicting Head of Ruler* (1973.37) was examined using HHXRF, SEM, and XRD.

Two HHXRF tests were run on this object. HHXRF spectral data shows Ca, Fe, and Al as minor components, and trace amounts of Na and Mg, suggesting some omphacite present (Additional file 1: Supplemental Table 1). Additionally, potassium (K) showed up as minor component, with one of the tests reporting the most amount of K out of all of the objects. The comparatively large amounts of K reported by the HHXRF suggest the presence of amazonite ($KAlSi_3O_3$) or muscovite ($KAl_2(AlSi_3O_{10})(OH)$). One analysis shows nearly equal amounts of Al and K; the near equal amounts make determining between which K containing mineral is present difficult, highlighting the importance of complementary techniques. Because of the trace amount of Na measured, the HHXRF analysis would indicate small amounts of jadeite. ROI analysis, however, grouped the object as jadeite for the Mg, Na, and Fe for both runs. The EDS elemental mapping (Fig. 6a) shows an even distribution of Fe and some phase separation between an Na–Al phase and an Mg–Ca phase, though Na, Al, Mg and Ca all are distributed throughout the map. The Na–Al heavier phase could be jadeite, and the Mg–Ca heavier phase could be omphacite. EDS composition measurements show nearly equal amounts of Na and Al (supporting the presence of jadeite), with traces of Mg, Ca, Fe, and K (Table 2). On EDS as well, object 1973.37 reported the highest percentage of K when compared to other objects. Amazonite is known to have twinning, which is not present in the SEM images [79]. From the EDS composition measurements, the % Jd equation predicts 90.12% Jd (Table 2), and the remaining amount is likely omphacite and the K rich mineral, given the other element percentages. This ratio of omphacite to jadeite estimated by EDS is contrary to the estimation made by HHXRF, with the HHXRF elemental analysis suggesting majority omphacite, but supported by ROI grouping. The EDS percentage does not match the XRF elemental percentages likely because the SEM/EDS analyzes a much smaller spot size than the XRF. Analyzing the XRD data in Fig. 6b, there is strong agreement of the 1973.37 pattern with omphacite, seen most prominently in the single peak at high d-spacing. There is matching for jadeite around 2.8–3.2, but this matching is mostly localized to that range, so the intensity of the peaks here likely does not suggest high jadeite content but reflect orientation effects which could cause these peaks to be more intense. In comparing the amazonite and muscovite patterns to the 1973.37 pattern there is good matching with muscovite, which helps determine that the K containing mineral that is present in the object is most likely muscovite. Looking at the macroscopic image (Fig. 6a), there is a clear distinction between a greyish color and the main green color. The gray appears to make up less of the object, so it could be the muscovite, and the green is likely a combination of jadeite and omphacite. Both XRD and HHXRF suggest majority omphacite composition, while EDS predicts majority jadeite. Due to the small spot size of EDS collection, the HHXRF and XRD data are likely more representative of the object as a whole, so it is concluded that the object is likely closer to an omphacite-jadeite classification with some muscovite present.

Bead depicting jaguar head (2008.82.4)

As illustrated in Fig. 7, the *Bead Depicting Jaguar Head* (2008.82.4) allowed for HHXRF and SEM analysis.

Two HHXRF tests were run on this object. Both of the HHXRF spectral data show Fe as major components and Al and Ca as minor components, with Na and Mg in trace amounts (Additional file 1: Supplemental Table 1). Of the two tests run, one showed minor components of K while the other showed trace amounts, with them averaging to be a minor component. This small amount of K could indicate the presence of amazonite or muscovite, but because of the inconsistent results, more testing is needed to support the relative amount present. Having Ca, Fe and Al as the largest components and trace Na suggests the presence of mostly omphacite with some jadeite. However, the ROI groups the object as jadeite for all included minerals. Similarly, the EDS compositional results show roughly equal parts Na and Al, suggesting jadeite (Table 2). Mg and Ca are present in minor amounts as well though, so EDS supports the presence of omphacite too. There are also trace amounts of Fe and even smaller amounts of K. The % Jd equation estimates 83.2% Jd (Table 2). The elemental mapping image does not show phase separation, just some carbon-rich area, which is likely some kind of organic matter on the object, as they were not cleaned before testing (Fig. 7). Again, the EDS only captures a small spot of the object and the HHXRF, which measures a larger area, did not measure the same area, which is why they may not agree. The elemental percent from the HHXRF did not agree with the ROI either. Because of this, it would be informative to take more EDS and HHXRF measurements from even more spots on the bead to be sure to collect from the different phases that are present. The elemental HHXRF information would suggest majority omphacite, though ROI and EDS suggest jadeite. From this, it can be concluded that this object is likely some combination of jadeite and omphacite. There is likely slightly less jadeite than predicted by the EDS (less than 80%), given the HHXRF information, so this object is determined to be

an omphacite-jadeite stone by the standards set by Gendron et al. [22] There is also likely some K containing mineral, either muscovite or amazonite, also present since K was found in varying amounts across EDS and HHXRF.

Bead depicting human head (2008.74)

As illustrated in Fig. 8 and Table 2, the *Bead Depicting Human Head* (2008.74) was only able to be analyzed with SEM/EDS.

The elemental map images show phase separation between a Na–Al phase, which could be jadeite and a phase with more Ca, likely omphacite. Fe appears evenly dispersed and not preferential to either phase. The elemental composition data shows roughly equal amounts of Na and Al, suggesting the presence of jadeite. However, there are trace amounts of Mg, Ca, and Fe, indicating the presence of omphacite is likely, probably being the other phase seen in the SEM image. From the % Jd equation, the object is estimated to be 81.8% Jd and the remaining is likely omphacite. Additionally, the elemental composition is similar to that of 2008.82.4, which was determined to be jadeite and omphacite. Therefore, this object is determined to be low purity jadeite with omphacite.

Figure (1969.23)

As illustrated in Fig. 9 and Table 2, the Figure (1969.23) was analyzed with the HHXRF, SEM, and XRD, due to its relatively small size.

HHXRF spectral data shows Ca as the largest major component, and Fe and Al as minor components. It also shows Mg and K in trace amounts and Na in nearly trace amounts. These fractions of Ca, Fe and Al would suggest omphacite as a dominant mineral type (Additional file 1: Supplemental Table 1). The near trace amounts of Na would suggest some small amount of jadeite. The trace amounts of K could indicate a small amount of amazonite or muscovite; it is likely amazonite due to the matching peaks in the XRD discussed below. ROI groups this object as jadeite for Mg and Fe, and omphacite for Na. The SEM image shows two defined phases, one composed of more Al–Ca which is likely an anorthite phase and one with more Mg–Fe–Na, which is likely an omphacite phase (Fig. 9a). Elemental compositions from EDS showed that the object has a low percentage of Na, which rules out it being majority jadeite based on EDS; the % Jd equation estimation supports this by yielding 41.07% Jd, the lowest amount of jadeite seen across all of the selected objects (Table 2). Ca is reported to be a minor component and the amount of Ca is roughly equal to that of Al. The presence of Mg and Fe in combination with Ca as major components would indicate the presence of omphacite. The high percentage of Ca and the ratio to Al would indicate the presence of another Ca containing minerals like anorthite. Lastly, the trace K would indicate presence of amazonite. From Gendron et al. [22], because the % Jd is between 20 and 80, the mineral type is considered to be omphacite based on EDS analysis.

Because of the curvature, the XRD peaks were shifted to the right by roughly 0.25 Å. After this shift, the pattern appears to match with many different minerals, with omphacite and jadeite peaks having relatively high intensity in the 2.8–3 Å range (Fig. 9b). The more prominent single peak, rather than two, at high d-spacing, suggests more omphacite present in this object than jadeite. The noise in this pattern made matching peaks more difficult, but there was matching of sufficiently high intensity peaks with amazonite, augite and anorthite between roughly 3–4.25 Å. As a result of the curvature, interpretation of the XRD spectra likely has error. Nonetheless, the XRD spectra indicates a mixture of omphacite, jadeite, anorthite, amazonite, and augite. Therefore, from all of the collected data, we determine this object to be majority omphacite with components of jadeite, anorthite, augite, and amazonite. Because of the variety of minerals that could be present, it would be beneficial to reanalyze the object, especially the XRD, on a flatter area of the object.

Need for multiple complimentary techniques

The use of multiple techniques for the identification of Mesoamerican greenstones has been successful in many other recent studies [29–31, 80] and was again productive in this study. Raman spectroscopy provided clear indications of the structural configuration and allowed for a rough quantification of the amount of jadeite and omphacite for the individual objects. In some cases, however, Raman spectra were difficult to interpret due to a number of factors including surface curvature and possible surface contamination. SEM with EDS provided a good overall impression of the surface microstructure and a good approximation of the elemental distribution of the phases, respectively, although these techniques were only possible for objects that met the size constraints of the sample chamber. The major advantage of SEM with EDS is that they could be used simultaneously allowing for an excellent understanding of the local microstructure, elemental distribution of the phases, including major and minoramounts of detectable elements present on object's surface, and a rough approximation of the amount of jadeite and omphacite present. XRD provided insight into the phases present and also allowed to a lesser extent than other techniques, the ability to approximate the amount of jadeite and omphacite present. The initial larger study [28] was aimed at testing the possibility of using HHXRF for mineralogical identification of various greenstones in museum and archaeological collections

with the use of a helium-flow meter to detect the lighter elements that are present in many of these stones (especially sodium and calcium). HHXRF, while cost effective and portable, does have limitations, especially in this case with the lack of a calibration that would produce parts per million (ppm) measurements for elemental composition that could then be compared to known and measured reference samples. But even with this limitation, our semi-quantitative results seem to support the findings of other techniques and show promise for future studies. HHXRF is not as precise as other techniques, but even using the methods in this study it can give general ideas about composition and also allow a more refined sampling strategy for more inaccessible characterization methods of a sample of objects. In summary, the collection of this data from the various complimentary techniques can assist in contributing to the development of databases and calibration curves for a broader understanding of jade and greenstone objects from Mesoamerican cultures and beyond, as these techniques continue to grow in the field of greenstone analysis.

Contextual interpretation

The only known source of jadeite in Mesoamerica is the Motagua valley of Guatemala [37, 81, 82], which is located within the Maya cultural region. Serpentine is more widely distributed in other parts of Mesoamerica (e.g., [83]) in addition to outcrops of serpentine in the Motagua valley where it occurs alongside jadeite deposits as they can form together [37]. It is not surprising then that the artifacts in the DMA collection that are identified as belonging to the Maya region show the highest numbers of jadeite objects as this cultural region is closest to the source of jadeite. While the Olmec heartland was located in the modern states of Veracruz and Tabasco in Mexico [6] Olmec influence during the Formative period was extensive [84] and contacts with the Maya region have been documented (e.g., [85–87]). The objects identified as Olmec or having Olmec influence in the DMA collection contain both jadeite and serpentine, further demonstrating this widespread influence and connection. Objects from cultures in Mexico somewhat further from the Maya region (i.e., Mixtec and Mezcala) were exclusively serpentine in this collection, although the sample size is small and it is known that both cultures worked a variety of greenstones (e.g., [88]). Also, while many have not been mineralogically characterized, Blomster [88] argues that serpentine and andesite were favored materials for Mezcala greenstone objects. Sourcing efforts for jadeite are complicated and tying artifacts to a specific location within the Motagua valley is not always possible due to extreme heterogeneity of trace elements in source outcrops [81]. This work is able to demonstrate that multiple methods can be used at least to differentiate various types of greenstones, which has recently been done for other museum collections (i.e., for the Dumbarton Oaks Collection [82]) and is valuable in terms of conservation and interpretation efforts for greenstone objects from around the world.

Conclusions

In this study, we examined a set of Mesoamerican jade and greenstone objects from the collection at the Dallas Museum of Art using multiple non-destructive techniques, including scanning electron microscopy with energy dispersive spectroscopy, Raman spectroscopy, X-ray diffraction, and handheld X-ray fluorescence spectroscopy. We briefly evaluated and discussed the advantages and disadvantages of each technique in the archaeological and historical context. Based on the results, most of the objects were identified to be a combination of jadeite and omphacite, while a few objects were determined to be in the serpentine family due to the higher presence of magnesium and sodium. These results further support the larger HHXRF study [28], which indicated that the DMA collections from the Maya, Olmec, and other Mesoamerican cultures often share jadeite and omphacite components, thus highlighting possible difficulties in attaining pure jadeite since omphacite and related minerals have similar color, hardness and luster properties and these minerals tend to form together and under similar conditions. Although the sample size is small, some regional patterns of resource use and procurement may be apparent. These patterns may be based on locational availability and regional spheres of influence, although more research is necessary. And while source attribution was not the goal of this study and is not possible at this time, using complementary scientific techniques for the differentiation of greenstones is worthwhile for museum conservation efforts, as well as aiding efforts of archaeological interpretation. These complementary methods are applicable for Mesoamerican contexts but can also be applied around the world.

Abbreviations

Am	Amazonite
Ant	Anorthite
Aug	Augite
DMA	Dallas museum of art
EDS	Energy dispersive X-ray spectroscopy
FTIR	Fourier-transform infrared spectroscopy
HHXRF	Handheld XRF
Inc	Inconclusive results
Jd	Jadeite
Jd-Om	Predominantly jadeite with omphacite
MURR	University of Missouri Research Reactor Center
Om-Jd	Predominantly omphacite with jadeite
Om	Omphacite

PIXE	Particle-induced X-ray emission
Ppm	Parts per million
ROI	Region of interest
SEM	Scanning electron microscopy
Serp	Serpentine
XRD	X-ray diffraction
XRF	X-ray fluorescence spectroscopy

Supplementary Information

The online version contains supplementary material available at https://doi.org/10.1186/s40494-023-01128-7.

Additional file 1. Supplemental Table 1: Description of Eight Greenstone Objectss Studied here from the Collections at the Dallas Museum of Art.

Additional file 2. Raw Data from Raman Spectroscopy including a Note about Non-destructive Testing.

Additional file 3. Artax2 Raw Data from HHXRF Spectroscopy.

Additional file 4. Raw Data from X-ray Diffraction Measurements.

Acknowledgements
The authors would like to thank NSF REU students, Maximiliano A. Burgess and Lissa Blackert, and graduate student, Silvia Briseno-Murguia, for experimental support and graduate student, Ben Sirota, and Professor Andrey Voevodin for help with portable Raman spectroscopy. The authors acknowledge funding from the National Science Foundation (NSF REU program—award 1461048) to initiate this project. The authors would also like to thank Kimberly Jones for experimental support and the invitation to complete the initial work. This work was performed in part at the University of North Texas's Materials Research Facility: A shared research facility for multi-dimensional fabrication and characterization and with the assistance of Drs. Saul Sepulveda and David Jaeger.

Author contributions
WK and FG analyzed and interpreted the data for the selected objects and contributed to writing the manuscript. MC collected and analyzed data as well as being a contributor to the writing of the manuscript. BK and DC analyzed the HHXRF data for the 67 objects from the DMA collection and were major contributors to the historical context and archaeological insight for the manuscript. MY was a contributor to the writing of the manuscript and assisted in data interpretation. ET and FB helped select and handle the objects for analysis, collect data and assisted with HHXRF. All authors read and approved the final manuscript.

Funding
The authors acknowledge funding from the National Science Foundation (NSF REU Program—Award 1461048).

Availability of data and materials
The datasets not presented but used and/or analyzed during the current study are available from the corresponding author on reasonable request.

Declarations

Competing interests
The authors declare that they have no competing interests.

Received: 14 July 2023 Accepted: 20 December 2023
Published online: 05 February 2024

References

1. Pohl MED, Pope KO, Von Nagy C. Olmec origins of Mesoamerican writing. Science. 1979;2002(298):1984–7.
2. Taube KA. The symbolism of jade in classic Maya religion. Anc Mesoam. 2005;16:23–50.
3. Pool CA. Olmec archaeology and early Mesoamerica. Cambridge: Cambridge University Press; 2007.
4. Jaime-Riverón O. Olmec greenstone in early formative mesoamerica: exchange and process of production. Anc Mesoam. 2010;21:123–33.
5. Coe MD, Diehl RA. In the land of the Olmec: the archaeology of San Lorenzo Tenochtitlán. Austin: University of Texas Press; 1980.
6. Diehl RA. The Olmecs: America's first civilization (ancient peoples and places), 1st ed. Thames and Hudson; 2005.
7. Clark JE, Pye ME. Olmec art and archaeology in Mesoamerica. National Gallery of Art, Center for Advanced Study in the Visual Arts; 2000.
8. Hobbs JM. The Jade Enigma. Gems Gemol. 1982;1982:3–19.
9. Lange FW. Precolumbian jade: new geological and cultural interpretations. Salt Lake City: University of Utah Press; 1993.
10. Delgado Robles AA, Sil JLR, Claes P, Manrique Ortega MD, González EC, Rojas MÁM, et al. Non-destructive in situ spectroscopic analysis of greenstone objects from royal burial offerings of the Mayan site of Palenque. Mexico Herit Sci. 2015;3:1–13.
11. Wang R, Li Y. Multiexcitation Raman spectroscopy in identification of Chinese jade. Spectrosc Lett. 2011;44:432–9.
12. Gendron F, Smith DC, Gendron-Badou A. Discovery of jadeite-jade in Guatemala confirmed by non-destructive Raman microscopy. J Archaeol Sci. 2002;29:837–51.
13. Middleton A, Ambers J. Case study: analysis of nephrite jade using Raman microscopy and X-ray fluorescence spectroscopy. In: Edwards HGM, Chalmers JM, editors. Raman spectroscopy in archeology and art history; 2005. p. 894–5.
14. Yin Z, Jiang C, Santosh M, Chen Y, Bao Y, Chen Q. Nephrite jade from Guangxi Province, China. Gems Gemol. 2014;50:228–35.
15. Jiang Y, Shi G, Xu L, Li X. Mineralogy and geochemistry of nephrite jade from Yinggelike deposit, Altyn Tagh (Xinjiang, NW China). Minerals. 2020;10:1–22.
16. Wang R, Zhang WS. Application of Raman spectroscopy in the nondestructive analyses of ancient Chinese jades. J Raman Spectrosc. 2011;42:1324–9.
17. Casadio F, Douglas JG, Faber KT. Noninvasive methods for the investigation of ancient Chinese jades: an integrated analytical approach. Anal Bioanal Chem. 2007;387:791–801.
18. Chen D, Yang Y, Qiao B, Li J, Luo W. Integrated interpretation of pXRF data on ancient nephrite artifacts excavated from Tomb No. 1 in Yuehe Town, Henan Province, China. Herit Sci. 2022;10:1–12.
19. Chen TH, Calligaro T, Pagès-Camagna S, Menu M. Investigation of Chinese archaic jade by PIXE and μRaman spectrometry. Appl Phys A Mater Sci Process. 2004;79:177–80.
20. Shen J. Nondestructive identification of gemstones by using a portable XRF–XRD system: an illuminating study for expanding its application in museums. SN Appl Sci. 2020;2:1–18.
21. Wang YY, Gan FX, Zhao HX. Nondestructive analysis of Lantian jade from Shaanxi Province, China. Appl Clay Sci. 2012;70:79–83.
22. Gendron F, Smith DC, Masson P, Rodríguez Martínez M del C, Ortiz Ceballos P. Portable Raman verification and quantification of jade in Olmec ceremonial axes from El Manatí, Veracruz, Mexico. J Raman Spectrosc. 2017;48:1618–32.
23. Manrique-Ortega MD, Mitrani A, Casanova-González E, Jiménez-Galindo LA, Ruvalcaba-Sil JL. Methodology for the non-destructive characterization of jadeite-jade for archaeological studies. Spectrochim Acta A Mol Biomol Spectrosc. 2019;217:294–309.
24. Kovacevich B, Callaghan MG. Fifty shades of green: interpreting Maya jade production, circulation, consumption, and value. Ancient Mesoamerica. 2019;30:457–72.
25. Kovacevich B, Neff H, Bishop RL. Laser ablation ICP-MS chemical characterization of jade from a jade workshop in Cancuen, Guatemala. In: Speakman RJ, Neff H, editors. Laser Ablation ICP-MS in archaeological research. Albuquerque: University of New Mexico Press; 2005.
26. Brigette Kovacevich. Chapter 3. In: Wells EC, Davis-Salazar KL, editors. Mesoamerican ritual economy archaeological and ethnological perspectives. Boulder: University Press of Colorado; 2007.
27. Meirelles ACR, Lima da Costa M. Mineralogy and chemistry of the green stone artifacts (muiraquitãs) of the museums of the Brazilian State of Pará. Geociências. 2012;65:59–64.

28. Kovacevich B, Crawford D, Carl M, Burgess MA, Young ML. Mesoamerican jades and greenstones from the dallas museum of art. Dallas Museum of Art Catalogue; 2022.
29. Manrique-Ortega MD, Claes P, Aguilar-Melo V, Wong-Rueda M, Ruvalcaba-Sil JL, Casanova-González E, et al. Non-invasive characterization of stone artifacts from the great temple of Tenochtitlan. Mexico MRS Proc. 2017;1656:293–307.
30. Garcia-Casco A, Knippenberg S, Rodríguez Ramos R, Harlow GE, Hofman C, Pomo JC, et al. Pre-Columbian jadeitite artifacts from the Golden Rock Site, St. Eustatius, Lesser Antilles, with special reference to Jadeitite artifacts from Elliot's, Antigua: implications for potential source regions and long-distance exchange networks in the Greater. J Archaeol Sci. 2013;40:3153–69.
31. Aguilar-Melo V, Mitrani A, Casanova-Gonzalez E, Manrique-Ortega MD, Pérez-Ireta G, Ruvalcaba-Sil JL, et al. Molecular and X-ray spectroscopies for noninvasive characterization of mayan green stones from bonampak. Chiapas Appl Spectrosc. 2019;73:1074–86.
32. Hammond NGL, Aspinall A, Feather SW, Hazelden J, Gazard T, Agrell SO. Maya Jade: Source Location and Analysis. In: Earle TK, Ericson JEBT, editors. San Diego: Academic Press; 1977. p. 35–67.
33. Miller ME, Taube KA. An illustrated dictionary of the gods and symbols of ancient Mexico and the Maya. New York: Thames and Hudson; 1997.
34. de Sahagun B. Chapter 9: The merchants. In: Anderson AJO, Dibble CE, editors. Florentine codex: general history of the things of new Spain. 2nd ed. Salt Lake City, Utah: School of American Research; 1959. p. 108.
35. de Sahagun B. Chapter 10: The people. In: Anderson AJO, Dibble CE, editors. Florentine codex: general history of the things of New Spain. 2nd ed. Salt Lake City, Utah: School of American Research; 1961. p. 108.
36. Taube K, Ishihara-Brito R. From stone to jewel: jade in ancient maya religion and rulership. In: Pillsbury J, Doutriaux M, Ishihara-Brito R, Tokovinine A, editors. Ancient Maya art at Dumbarton Oaks. Washington, DC: Dumbarton Oak; 2012.
37. Harlow GE. Middle American Jade: geological and petrologic perspectives on variability and source. Precolumbian Jade: New Geological and Cultural Interpretations. Salt Lake City: University of Utah Press; 1993. p. 11–30.
38. Lahanier C, Preusser FD, Van Zelst L. Study and conservation of museum objects: use of classical analytical techniques. Nucl Inst Methods Phys Res B. 1986;14:1–9.
39. Young ML. Archaeometallurgy using synchrotron radiation: a review. Rep Prog Phys. 2012;2012:75.
40. Harlow GE, Berman MJ, Cárdenas Párraga J, Hertwig A, García-Casco A, Gnivecki PL. Pre-Columbian jadeitite artifacts from San Salvador Island, Bahamas and comparison with jades of the eastern Caribbean and jadeitites of the greater Caribbean region. J Archaeol Sci Rep. 2019;26:101830.
41. Mitrani Viggiano A, Ruvalcaba Sil JL, Manrique Ortega MD, Corregidor BV. Non-destructive micro-chemical and micro-luminescence characterization of jadeite. Microsc Microanal. 2016;22:1304–15.
42. Brueckner HK, Avé Lallemant HG, Sisson VB, Harlow GE, Hemming SR, Martens U, et al. Metamorphic reworking of a high pressure-low temperature mélange along the Motagua fault, Guatemala: a record of Neocomian and Maastrichtian transpressional tectonics. Earth Planet Sci Lett. 2009;284:228–35.
43. Harlow GE, Flores KE, Marschall HR. Fluid-mediated mass transfer from a paleosubduction channel to its mantle wedge: evidence from jadeitite and related rocks from the Guatemala Suture Zone. Lithos. 2016;258–259:15–36.
44. Flores KE, Martens UC, Harlow GE, Brueckner HK, Pearson NJ. Jadeitite formed during subduction: in situ zircon geochronology constraints from two different tectonic events within the Guatemala Suture Zone. Earth Planet Sci Lett. 2013;371–372:67–81.
45. Yui TF, Maki K, Usuki T, Lan CY, Martens U, Wu CM, et al. Genesis of Guatemala jadeitite and related fluid characteristics: Insight from zircon. Chem Geol. 2010;270:45–55.
46. Martens UC, Brueckner HK, Mattinson CG, Liou JG, Wooden JL. Timing of eclogite-facies metamorphism of the Chuacús complex, Central Guatemala: record of Late Cretaceous continental subduction of North America's sialic basement. Lithos. 2012;146–147:1–10.
47. Guo B, Zhu X, Dong A, Yan B, Shi G, Zhao Z. Mg isotopic systematics and geochemical applications: a critical review. J Asian Earth Sci. 2019;176:368–85.
48. Simons KK, Harlow GE, Brueckner HK, Goldstein SL, Sorensen SS, Hemming NG, et al. Lithium isotopes in Guatemalan and Franciscan HP-LT rocks: insights into the role of sediment-derived fluids during subduction. Geochim Cosmochim Acta. 2010;74:3621–41.
49. Nasdala L, Smith DC, Kaindl R, Ziemann MA. Raman spectroscopy: analytical perspectives in mineralogical research. EMU Notes Mineral. 2004;6:1–63.
50. Hernández-Murillo C, García-Piedra S, Alfaro-Córdoba M, Fernández-Esquivel P, Ménager M, Montero ML. Influence of surface roughness on the spectroscopic characterization of jadeite and greenstones archaeological artifacts: the axe-god pendants case study. Spectrochim Acta A Mol Biomol Spectrosc. 2022;2022:267.
51. Smith DC, Gendron F. Archaeometric application of the Raman microprobe to the non-destructive identification of two pre-columbian ceremonial polished "greenstone" axe-heads from Mesoamerica. J Raman Spectrosc. 1997;28:731–8.
52. Heginbotham A, Bezur A, Bouchard M, Davis JM, Eremin K, Frantz JH, Glinsman L, Hayek L-AC, Hook D, Kantarelou V, Karydas AG, Lee L, Mass J, Matsen C, McCarthy B, Mc RJ. An evaluation of inter-laboratory reproducibility for quantitative XRF of historic copper alloys. In: Mardikian P, Chemello C, Watters C, Hull P, editors. Metal 2010: international conference on metal conservation, interim meeting of the international council of museums committee for conservation metal working group. Charleston, South Carolina, USA: Clemson University; 2010. p. 178–88.
53. Bronk H, Röhrs S, Bjeoumikhov A, Langhoff N, Schmalz J, Wedell R, et al. ArtTAX—a new mobile spectrometer for energy-dispersive micro X-ray fluorescence spectrometry on art and archaeological objects. Fresenius J Anal Chem. 2001;371:307–16.
54. Vittiglio G, Janssens K, Vekemans B, Adams F, Oost A. Compact small-beam XRF instrument for in-situ analysis of objects of historical and/or artistic value. Spectrochim Acta Part B At Spectrosc. 1999;54:1697–710.
55. Potts PJ, Ellis AT, Kregsamer P, Streli C, Vanhoof C, West M, et al. Atomic spectrometry update—X-ray fluorescence spectrometry. J Anal At Spectrom. 2006;21:1076–107.
56. Malmqvist KG. Comparison between PIXE and XRF for applications in art and archaeology. Nucl Inst Methods Phys Res B. 1986;14:86–92.
57. Ardid M, Ferrero JL, Juanes D, Lluch JL, Roldán C. Comparison of total-reflection X-ray fluorescence, static and portable energy dispersive X-ray fluorescence spectrometers for art and archeometry studies. Spectrochim Acta Part B At Spectrosc. 2004;59:1581–6.
58. Janssens K, Vittiglio G, Deraedt I, Aerts A, Vekemans B, Vincze L, et al. Use of microscopic XRF for non-destructive analysis in art and archaeometry. X-ray Spectrom. 2000;29:73–91.
59. Mantler M, Klikovits J. Analysis of art objects and other delicate samples: Is XRF really nondestructive? Powder Diffr. 2004;19:16–9.
60. Mantler M, Schreiner M. X-ray fluorescence spectrometry in art and archaeology. X-ray Spectrom. 2000;29:3–17.
61. Shugar AN, Mass JL. Handheld XRF for art and archaeology. Shugar AN, Mass JL, editors. Leuven: Leuven University Press; 2012.
62. Juárez-Rodríguez O, Argote-Espino D, Santos-Ramírez M, López-García P. Portable XRF analysis for the identification of raw materials of the Red Jaguar sculpture in Chichén Itzá, Mexico. Quat Int. 2018;483:148–59.
63. Millhauser JK, Rodríguez-Alegría E, Glascock MD. Testing the accuracy of portable X-ray fluorescence to study Aztec and Colonial obsidian supply at Xaltocan, Mexico. J Archaeol Sci. 2011;38:3141–52.
64. Shackley MS. X-ray fluorescence spectrometry (XRF) in geoarchaeology. X-ray Fluorescence Spectrometry (XRF) in Geoarchaeology; 2011.
65. De Ryck I, Adriaens A, Pantos E, Adams F. A comparison of microbeam techniques for the analysis of corroded ancient bronze objects. Analyst. 2003;128:1104–9.
66. Young ML, Casadio F, Schnepp S, Almer J, Haeffner DR, Dunand DC. Synchrotron X-ray diffraction and imaging of ancient Chinese bronzes. Appl Phys A Mater Sci Process. 2006;83:163–8.
67. Carl M, Young ML. Complementary analytical methods for analysis of Ag-plated cultural heritage objects. Microchem J. 2016;126:307–15.
68. Young ML, Casadio F, Marvin J, Chase WT, Dunand DC. An ancient Chinese bronze fragment re-examined after 50 years: contributions from modern and traditional techniques. Archaeometry. 2010;52:1015–43.
69. Sciau P, Goudeau P. Ceramics in art and archaeology: a review of the materials science aspects. Eur Phys J B. 2015;2015:88.

70. Sciau P, Salles P, Roucau C, Mehta A, Benassayag G. Applications of focused ion beam for preparation of specimens of ancient ceramic for electron microscopy and synchrotron X-ray studies. Micron. 2009;40:597–604.
71. Drake L. https://www.xrf.guru/; 2018.
72. Migliori A, Bonanni P, Carraresi L, Grassi N, Mandò PA. A novel portable XRF spectrometer with range of detection extended to low-Z elements. X-ray Spectrom. 2011;40:107–12.
73. Ferguson JR. X-ray fluorescence of obsidian: approaches to calibration and the analysis of small samples. In: Shugar AN, Mass JL, editors. Studies in achaeological sciences 3: handheld XRF for art and archaeology. Leuven: Leuven University Press; 2012. p. 401–22.
74. Craig N, Speakman RJ, Popelka-Filcoff RS, Glascock MD, Robertson JD, Shackley MS, et al. Comparison of XRF and PXRF for analysis of archaeological obsidian from southern Perú. J Archaeol Sci. 2007;34:2012–24.
75. Vicenzi E, Sharps M, Lam T. Quantitative analysis of obsidian and determination of source provenance using an analytical dual beam SEM. Microsc Microanal. 2021;27:2560–3.
76. Lafuente B, Downs RT, Yang H, Stone N. The power of databases: the RRUFF project. In: Armbruster T, Danisi RM, editors. Highlights in mineralogical crystallography. De Gruyter (O); 2015. p. 1–30.
77. JADE Standard (Computer software), Materials Data. Livermore, CA, USA; 2019.
78. Yang H, Konzett J, Frost DJ, Downs RT. X-ray diffraction and Raman spectroscopic study of clinopyroxenes with six-coordinated Si in the Na(Mg0.5Si0.5)Si 2O6-NaAlSi2O6 system. Am Mineral. 2009;94:942–9.
79. https://www.mineralminers.com/html/amzminfo.htm. Gem & Mineral Miners, Inc.; 2020.
80. Viggiano AM, Sil JLR, Ortega MDM, Berdasco VC. Non-destructive microchemical and micro-luminescence characterization of jadeite. Microsc Microanal. 2016;22:1304–15.
81. Niespolo EM. Mineralogy, geochemistry, and stable isotopes of Guatemalan Jadeitites. Long Beach: California State University; 2014.
82. Lauffenburger J, Cockrell BR, Gates G, Hoopes JW, Kovacevich B, Mora Marin D. A noninvasive approach to the study of jade artifacts from Central America. In Pre-Columbian Central America, Colombia, and Ecuador Toward an Integrated Approach. McEwan C, Cockrell B, Hoopes J, editors. Dumbarton Oaks Research Library and Collection; 2021.
83. Rosenswig RM. The beginnings of Mesoamerican civilization. Cambridge: Cambridge University Press; 2009.
84. Inomata T, Fernandez-Diaz JC, Triadan D, García Mollinedo M, Pinzón F, García Hernández M, et al. Origins and spread of formal ceremonial complexes in the Olmec and Maya regions revealed by airborne lidar. Nat Hum Behav. 2021;5:1487–501.
85. Reilly FK III. Olmec iconographic influences on the symbols of Mayan Rulership: an examination of possible sources. In: 6th Palenque round table; 1986. p. 151–66.
86. Šprajc I, Inomata T, Aveni AF. Origins of Mesoamerican astronomy and calendar: evidence from the Olmec and Maya regions. Sci Adv. 2023;2023:9.
87. Blomster JP. Commensalism, imaginaries and early urbanism: a Mezcala Sculpture in the Mixteca Alta, Mexico. Camb Archaeol J. 2022;32:601–18.
88. Domenici D. Rediscovery of a Mesoamerican greenstone sculpture from the collection of Ulisse Aldrovandi. J Hist Collect. 2022;34:1–22.

Publisher's Note